

NIST GCR 97-710

**ANALYSIS OF PARTIALLY GROUTED
MASONRY SHEAR WALLS**

**FILE COPY
DO NOT TAKE**

Building and Fire Research Laboratory
Gaithersburg, Maryland 20899

United States Department of Commerce
Technology Administration
National Institute of Standards and Technology

ANALYSIS OF PARTIALLY GROUTED MASONRY SHEAR WALLS

Prepared for

U. S. Department of Commerce
National Institute of Standards and Technology
Building and Fire Research Laboratory
Gaithersburg, MD 20899

By

P. Benson Shing
Li Cao

Department of Civil, Environmental & Architectural Engineering
University of Colorado at Boulder
Boulder, CO 80309-0428

March 1997

Contract No. 43NANB513421



U.S. Department of Commerce
William M. Daley, *Secretary*
Technology Administration
Mary L. Good, *Under Secretary for Technology*
National Institute of Standards and Technology
Arati Prabhakar, *Director*

A PC based version of the finite element program FEAP incorporating the elements presented in this report is not available at present. The PC based version and a user's manual are being developed by the principal investigator, Dr. P. Benson Shing, University of Colorado at Boulder.

ABSTRACT

Six partially grouted reinforced masonry shear walls that were tested at NIST are analyzed in this study. The main aim of the study is to assess the capability of some state-of-the-art finite element models in predicting the behavior of these wall specimens under cyclic in-plane lateral loads. To this end, two types of elements are used to model the behavior of a partially grouted masonry wall to reflect the inhomogeneity and anisotropy introduced by mortar joints. The shear and tensile behavior of a mortar joint is modeled with plasticity-based interface elements, while the fracture behavior of masonry units is modeled with smeared crack elements. The analyses have been carried out in several stages. First, a pretest analysis was conducted on one of the wall specimens. This was followed by an extensive parametric study to identify the sensitivity of numerical results to the modeling parameters. Finally, the finite element models have been fine tuned with data obtained from relevant material tests that were conducted in conjunction with the tests of the wall specimens. The main variables in the wall specimens are the aspect ratio of the walls and the quantity of horizontal reinforcement. It has been shown that the behavior of a partially grouted reinforced masonry wall is very similar to that of a reinforced concrete infilled frame. The grouted masonry provides the frame action while the ungrouted masonry acts like infill panels. The numerical results show that the quantity of the horizontal steel in the bond beam has little influence on the behavior of the wall specimens. The walls with a low aspect ratio tend to exhibit a distinct sliding shear failure through the bed joints at mid-height, while those with a higher aspect ratio have more severe cracking in the vertical joints within the wall panels. The vertical cracks between the grouted and ungrouted cells are reasonably well captured in the analyses. However, except for one wall specimen, the lateral strengths obtained in the analyses are higher than those shown by the experiments. The discrepancies in the numerical and experimental load-displacement curves can be partly caused by the different load histories and partly by the discrepancy in the bond strength between the wall panels and the concrete head beams.

ACKNOWLEDGMENTS

The funding for this study was provided by the National Institute of Standards and Technology. The cooperation and continuous support provided by Dr. Arturo Schultz, formerly at NIST, and Dr. Riley M. Chung of NIST in this project are gratefully acknowledged. However, opinions expressed in this report are those of the writers and do not necessarily represent those of the sponsor.

TABLE OF CONTENTS

ABSTRACT	i
ACKNOWLEDGMENTS	ii
TABLE OF CONTENTS	iii
1. INTRODUCTION	1
2. WALL SPECIMENS ANALYZED	2
3. FINITE ELEMENT MODELS	2
3.1. Masonry Units	3
3.2. Mortar Joints	4
3.3. Reinforcing Bars	6
3.4. Models of Wall Specimens	6
3.5. Model Calibration	7
3.6. Sensitivity Analysis	10
4. NUMERICAL RESULTS	12
5. CORRELATION OF EXPERIMENTAL AND NUMERICAL RESULTS	13
6. CONCLUSIONS	15
7. REFERENCES	16
8. FIGURES	18

ANALYSIS OF PARTIALLY GROUTED MASONRY SHEAR WALLS

1. INTRODUCTION

An experimental research program has been carried out at NIST to study the seismic resistance of partially grouted reinforced masonry shear walls [6]. The main intent of this program is to investigate the feasibility of using partially grouted masonry construction in regions of moderate seismicity, where full grouting may not be necessary. Partial grouting is perceived to be economically more competitive than full grouting, and is, therefore, preferred by the construction industry. As part of this program, the University of Colorado is asked to assess the capability of some state-of-the-art finite element models in predicting the behavior of partially grouted masonry shear walls subjected to cyclic in-plane lateral loads.

Smeared crack finite element models have been used in a number of studies to evaluate the lateral resistance of fully grouted reinforced masonry shear walls [1,2] based on the same approach used in reinforced concrete analysis. While the behavior of a fully grouted reinforced masonry structure is very similar to that of a reinforced concrete structure, the use of smeared crack models in such analysis has a number of limitations. It has been shown that a smeared crack model is not able to capture the brittle shear behavior of a masonry wall panel because of an unrealistic kinematic constraint introduced by the smeared crack assumption [2]. In a smeared crack model, a crack medium is approximately represented by an equivalent continuum, which tends to introduce an unrealistic diagonal compression field and, thereby, a spurious shear resistance in a wall panel. In addition, mortar joints are the inherent planes of weakness in a partially grouted masonry wall, and, therefore, the failure of such a wall is expected to be dominated by the fracture of these joints. Hence, one cannot realistically model partially grouted masonry as a homogenous isotropic continuum, which is often assumed for fully grouted masonry. Because of this, the use of smeared crack elements alone is expected to introduce additional problems in the analysis of partially grouted masonry walls.

In this study, two types of elements are used to model the behavior of a partially grouted masonry wall to reflect the inhomogeneity and anisotropy introduced by mortar joints. The shear and tensile behavior of a mortar joint is modeled with plasticity-based interface elements, while the fracture behavior of masonry units is modeled with smeared crack elements. These elements are used to analyze six partially grouted wall specimens that were tested at NIST. The analyses have been carried out in several stages. First, a pretest analysis was conducted on one of the wall specimens. This was followed by an extensive parametric study to identify the sensitivity of numerical results to the modeling parameters. Finally, the finite element models have been fine-tuned with data obtained from relevant material tests conducted in conjunction with the wall specimens. This report summarizes the finite element formulations and models used in the analyses, the calibration of the models, the failure mechanisms predicted by the analyses, and the correlation of numerical and experimental results.

2. WALL SPECIMENS ANALYZED

Six wall specimens that were tested at NIST are analyzed here. These specimens are designated as Walls No. 1, 3, 5, 7, 9, and 11 in the report by Schultz [6]. The design of a typical wall specimen is shown in Fig. 1 and their dimensions are shown in Fig. 2. Each specimen was partially grouted, with two exterior columns of grouted cells and a grouted bond beam at mid-height. The grouted cells were reinforced with standard deformed bars. The design variables in these specimens include the quantity of horizontal reinforcement in the bond beams and the length of the wall panels, as shown in Table 1. The test setup is shown in Fig. 3. The top and bottom of each specimen were prevented from rotation. The vertical compressive stress applied to each specimen was targeted at 1.38 MPa, with the compressive forces actually applied in the tests shown in Table 1. The wall specimens were subjected to cyclic lateral loads. A detailed description of the experimental program can be found in Ref. 6.

3. FINITE ELEMENT MODELS

In the finite element analysis conducted here, masonry is treated as a composite material, in which the mortar joints and units are modeled individually with different types of elements. The masonry units are modeled with smeared crack elements, which account for both tensile and

compressive fracture of the units, while the mortar joints are modeled with interface elements to account for the inherent planes of weakness. The reinforcing steel is modeled as a smeared overlay on top of smeared crack elements. These models are summarized in the following sections.

Table 1 - Wall Specimens

Wall Spec.	Height (H) (mm)	Length (L) (mm)	Nominal Width (mm)	Aspect ratio (H/L)	Vertical Reinf. Ratio (%)	Horizontal Reinf. Ratio (%)	Axial Compression (kN)
1	1422	2845	203	0.5	0.4	0.05	267
3	1422	2032	203	0.7	0.4	0.05	191
5	1422	1422	203	1.0	0.4	0.05	133
7	1422	2845	203	0.5	0.4	0.12	262
9	1422	2032	203	0.7	0.4	0.12	177
11	1422	1422	203	1.0	0.4	0.12	132

3.1. Masonry Units

A plane-stress smeared crack formulation is used to model the behavior of masonry units. In this formulation, it is assumed that cracks are smeared over an entire element. The properties of the units are assumed to be homogeneous and isotropic before cracking. The compressive failure and tensile fracture of masonry are governed by a von Mises failure surface with a Rankine-type tension cutoff as shown in Fig. 4, in which σ_1 and σ_2 are the principal stresses, f'_m and f'_t are the compressive and tensile strengths of masonry, and f_o determines the initial yield surface which is also governed by the von Mises criterion. Before the tension cutoff surface is reached, the material is assumed to be elastic-plastic, of which the plastic behavior is represented by J_2 plasticity as soon as the stress state reaches the initial yield surface. The material exhibits a strain-hardening behavior when the stress state is between the initial yield surface and the final failure surface. Strain softening occurs once the final yield surface is reached. The von Mises failure criterion can be expressed as follows.

$$J_2 - \sigma_e^2(\varepsilon_p) = 0 \quad (1)$$

in which J_2 is the second invariant of the deviatoric stress, and σ_e and ε_p represent the effective stress and effective plastic strain, respectively. The strain hardening/softening rules in the plasticity model are specified in terms of the effective stress (σ_e)-effective plastic strain (ε_p)

relation shown in Fig. 5, where the effective plastic strain is defined as $\varepsilon_p = \int \sqrt{\frac{2}{3}} d\varepsilon_{ij}^p d\varepsilon_{ij}^p$ with ε_{ij}^p being the plastic strain expressed in indicial notations.

Tensile cracking occurs when the tension-cutoff surface is reached. This transforms the material behavior from elastic-plastic to nonlinear orthotropic with the axes of orthotropy ($t-n$) parallel and perpendicular to the crack, as shown in Fig. 6. A coaxial rotating crack formulation is used so that the crack remains perpendicular to the direction of the maximum principal strain. The coaxiality of the principal axes of stress and strain is maintained by expressing the postcracked shear modulus, G , as a function of the principal stresses and principal strains as follows: $G = (\sigma_1 - \sigma_2)/[2(\varepsilon_1 - \varepsilon_2)]$. The tensile and compressive stress-strain relations of the orthotropic model are shown in Fig. 7. From the consistency standpoint, the curve in Fig. 7(a) should be calibrated in such a way that it reflects the uniaxial compressive behavior prescribed in Fig. 5. The details of the smeared crack model can be found in Ref. 2.

3.2. Mortar Joints

An elastic-plastic interface model developed by Lotfi and Shing [3] is used to simulate the behavior of mortar joints and the vertical splitting of masonry units. The elastic normal and shear stiffnesses, D_{nn} and D_{tt} , of an interface are assumed to be constant, and elastic shear dilatation is ignored. The yield surface of an interface is represented by a hyperbolic function, as shown in Fig. 8. This yield function can be expressed as follows.

$$F(\sigma, \mathbf{q}) = \tau^2 - \mu^2(\sigma - s)^2 + 2r(\sigma - s) = 0 \quad (2)$$

in which $\boldsymbol{\sigma} = \{\sigma, \tau\}^T$, $\mathbf{q} = \{r, s, \mu\}^T$, σ is the normal stress and τ is the shear stress in the interface, r is the radius of curvature of the yield surface at the vertex of the hyperbola, s is tensile strength of the interface, and μ is the slope of the asymptotes of the hyperbola. The cohesion, as defined in Fig. 8, can be expressed as $c = \sqrt{2sr + (\mu s)^2}$. The loss of cohesion and frictional resistance is governed by a set of work softening rules when the stress state reaches the initial yield surface. The change of the yield surface is governed by the evolution of the internal variables \mathbf{q} as follows.

$$s = s_o \left(1 - \frac{\kappa_1}{G_f^I} - \frac{\kappa_2}{G_f^{II}}\right) \geq 0 \quad (3)$$

$$r = r_r + (r_o - r_r)e^{-\beta\kappa_3} \quad (4)$$

$$\mu = \mu_r + (\mu_o - \mu_r)e^{-\alpha\kappa_3} \quad (5)$$

in which G_f^I and G_f^{II} are energies related to mode-I and mode-II fracture, respectively, r_o and μ_o are the initial values and r_r and μ_r are the residual values of r and μ , α and β are parameters that control the rate of work softening, and κ_i 's are parameters related to the plastic work generated by the relative displacement of the interface and are defined as follows.

$$\dot{\kappa}_1 = \langle \sigma \rangle \dot{d}_n^p \quad (6)$$

$$\dot{\kappa}_2 = [\tau - \tau_{r1} \text{sign}(\tau)] \dot{d}_t^p \quad (7)$$

$$\dot{\kappa}_3 = (\tau_{r1} - \tau_{r2}) \text{sign}(\tau) \dot{d}_t^p \quad (8)$$

in which $\langle \cdot \rangle$ = Macauley brackets, \dot{d}_n^p and \dot{d}_t^p are the relative plastic displacements of the interface in the normal and tangential directions, respectively, $\tau_{r1}^2 = \mu^2 \sigma^2 - 2r\sigma$, and $\tau_{r2}^2 = \mu_r^2 \sigma^2 - 2r_r\sigma$. The physical meaning of the last two parameters are illustrated in Fig. 9. They define the residual yield surfaces when the tensile strength of the interface is exhausted.

A non-associated flow rule is adopted here with the plastic potential expressed as

$$Q(\sigma, \mathbf{q}) = \eta \tau^2 + (r - r_r)(\sigma - s) \quad (9)$$

in which η is a parameter that controls dilatancy.

The interface constitutive model has been implemented in a double-noded isoparametric line element as shown in Fig. 10.

3.3. Reinforcing Bars

Reinforcing bars are modeled as an elastic-hardening plastic material by means of a smeared overlay on top of a smeared crack element. It is assumed that there is no bond slip between the reinforcing bars and concrete. A uniaxial stress-strain relation is considered for each reinforcing direction.

3.4. Models of Wall Specimens

The finite element discretization of the masonry wall specimens is shown in Fig. 11. The finite element model consists of concrete header and footer beams and a masonry panel. Four-node quadrilateral smeared crack elements are used to represent masonry units. The concrete beams are modeled with elastic plane stress elements since they are not expected to fail in the tests. To account for the stiffening effect of the steel head beams at the top and bottom of each specimen and the concrete spacer beam beneath the footer beam, as shown in Fig. 3, the modulus of elasticity of the concrete beams is deliberately increased to 730 GPa, which is way beyond that of the concrete. Each masonry unit is divided into two elements with an interface element in between. The interface is to allow the splitting of masonry units, which is often observed in actual tests but cannot be captured in a smeared crack model. The interface permits a mixed-mode fracture as described in a previous section. The mortar joints and the joints between the masonry panel and concrete beams are modeled with interface elements as well. The reinforcing bars in the grouted cells are modeled with a smeared steel overlay on top of smeared crack elements. The steel is assumed to be elastic-perfectly plastic. They are located in the two exterior

columns of grouted cells and also in the bond beam at the mid-height of a wall, which are shown in Fig. 1.

The top and bottom beams are prevented from rotation in the analyses as in actual tests. The analyses are carried out with displacement control under a monotonically increasing lateral displacement and a constant vertical compressive load. The nonlinear analysis is performed with a modified Newton iteration based on the initial elastic stiffness of the structure.

3.5. Model Calibration

In the calibration of the finite element models, two types of masonry units, three types of mortar joints, and one internal interface are considered. These are the grouted and ungrouted masonry units in a partially grouted wall, the bed joints in grouted and ungrouted masonry, the head joints, and the vertical interface within a unit.

The calibration of smeared crack elements requires information on the uniaxial stress-strain relation of masonry. To this end, the compressive strengths of air-cured masonry prisms that were prepared with the wall specimens and were tested on the same days as the corresponding walls are used. Since the prism tests provide only the compressive strengths, the tensile strengths and elastic moduli of masonry have to be estimated from empirical formulas. It is assumed that the tensile strength, f'_t , is equal to $4\sqrt{f'_m}$, where f'_m is the compressive strength of masonry as indicated in Fig. 4. The stress, f_o , at which plastic deformation initiates is assumed to be $0.5f'_m$. The elastic modulus, E_m , of masonry is estimated with the formula recommended in the Uniform Building Code [9] and the shear modulus $G = E_m/[2(1 + \nu)]$, where ν is the Poisson's ratio, which is assumed to be 0.2. Other parameters of the smeared crack model, prescribing the strain at the peak stress and the post-peak behavior of masonry, can be calibrated only if the complete compressive stress-strain relation of the masonry is available. Hence, their values can only be roughly estimated in this study based on recommendations provided in Ref. 2 on similar materials. The values of the key modeling parameters selected here are summarized in Table 2. They are based on the net cross-sectional area of masonry, with the net widths of the grouted and ungrouted masonry indicated in the table. The residual strain

resulting from unloading in the tension region, which is governed by γ as shown in Fig. 7(b), is assumed to be zero.

Table 2 - Calibration of Smeared Crack Elements for Masonry Units

Wall Spec.	Mason. Units ¹	E_m (GPa)	G (GPa)	ν	f_o (MPa)	f'_m (MPa)	f'_t (MPa)	ε_{1p}	ε_{2p}	α_1 (MPa)	Width (mm)
1	UG	14.7	6.13	0.2	9.80	19.6	1.45	0.002	0.003	6.98	68
	G	15.8	6.54	0.2	10.5	21.0	1.51	0.002	0.003	6.98	193
3	UG	13.8	5.72	0.2	9.20	18.4	1.44	0.002	0.003	6.98	68
	G	16.9	7.03	0.2	11.2	22.4	1.58	0.002	0.003	6.98	193
5	UG	15.4	6.41	0.2	10.3	20.6	1.51	0.002	0.003	6.98	68
	G	14.6	6.06	0.2	9.75	19.5	1.45	0.002	0.003	6.98	193
7	UG	12.1	5.10	0.2	8.10	16.2	1.31	0.002	0.003	6.98	68
	G	15.3	6.41	0.2	10.2	20.4	1.51	0.002	0.003	6.98	193
9	UG	13.6	5.65	0.2	9.00	18.0	1.41	0.002	0.003	6.98	68
	G	13.7	5.72	0.2	9.10	18.2	1.42	0.002	0.003	6.98	193
11	UG	14.7	6.13	0.2	9.80	19.6	1.45	0.002	0.003	6.98	68
	G	14.3	5.99	0.2	9.55	19.1	1.45	0.002	0.003	6.98	193

¹G: Grouted; UG: UngROUTed

No information is available on the tensile and shear behavior of the masonry bed joints. The behavior of bed joints in grouted masonry is very much governed by the properties of the grout, while that in ungrouted masonry depends, to a large extent, on the interface between the mortar and masonry units. Such behavior can be assessed by subjecting masonry joints to shearing tests [4,5]. However, in the absence of such data, the calibration of interface elements is based on information provided in a prior study [5], in which direct shear tests were conducted on similar mortar joints. The elastic interface stiffnesses, D_{nn} and D_{tt} , are set to be very high to prevent the penetration of smeared crack elements and to match the elastic lateral stiffness of the wall specimens obtained in the tests. The tensile strength of the bed joints in grouted masonry is assumed to be the same as that of the grouted units, while that in ungrouted masonry is assumed to be $0.05 f'_m$, where f'_m is the compressive strength of the hollow units. The fracture of mortar joints in ungrouted masonry often occurs at the interface between the mortar and masonry units,

and rarely in the mortar layer itself. Hence, this fracture strength is usually lower than those of the mortar and units themselves. For this reason, the fracture strength of these joints is conservatively estimated to be $0.05 f'_m$. Other parameters, which are related to the fracture energies, softening, and dilatancy, are based on data obtained in Ref. 5. The values adopted here are summarized in Table 3, which are based on the net cross-sectional area of a joint. The net width of a bed joint is the same as that of the corresponding masonry unit, which is shown in Table 2.

Table 3 - Calibration of Interface Elements for Masonry Bed Joints

Wall Spec.	Mason. Units ¹	D_{nn}, D_{tt} (MPa/mm)	s_o (MPa)	G_f' (N/mm)	G_f'' (N/mm)	μ_o (MPa)	μ_r (MPa)	α, β (mm/N)	r_o (kPa)	r_r (kPa)	η
1	UG	136	0.98	0.123	0.613	0.95	0.60	11.4	68.9	34.4	0.1
	G	136	1.51	0.123	0.613	0.95	0.60	11.4	68.9	34.4	0.1
3	UG	136	0.92	0.123	0.613	0.95	0.60	11.4	68.9	34.4	0.1
	G	136	1.58	0.123	0.613	0.95	0.60	11.4	68.9	34.4	0.1
5	UG	136	1.03	0.123	0.613	0.95	0.60	11.4	68.9	34.4	0.1
	G	136	1.45	0.123	0.613	0.95	0.60	11.4	68.9	34.4	0.1
7	UG	136	0.81	0.123	0.613	0.95	0.60	11.4	68.9	34.4	0.1
	G	136	1.51	0.123	0.613	0.95	0.60	11.4	68.9	34.4	0.1
9	UG	136	0.90	0.123	0.613	0.95	0.60	11.4	68.9	34.4	0.1
	G	136	1.42	0.123	0.613	0.95	0.60	11.4	68.9	34.4	0.1
11	UG	136	0.98	0.123	0.613	0.95	0.60	11.4	68.9	34.4	0.1
	G	136	1.45	0.123	0.613	0.95	0.60	11.4	68.9	34.4	0.1

¹G: Grouted; UG: UngROUTed

The properties of the head joints are assumed to be the same as those of ungrouted bed joints. The continuity of the grout across the head joints was expected to be poor in the bond beams and, hence, the grouted area is ignored in the head joints. The width of a head joint is assumed to be 51 mm based on the area covered with mortar in standard construction practice. However, it is later found that the bond beam units used had exceptionally large cavities that were as wide as 100 mm. In spite of this, a numerical parametric study, presented later on, indicates that the strength of head joints have little influence on the lateral resistance of a wall.

For this reason, this width is not revised in the analyses. The vertical interface within a unit is assumed to have the same properties as the head joints except that its tensile strength is assumed to be the same as that of the hollow units. The properties of the vertical interfaces in grouted and ungrouted units are assumed to be the same, but the widths are different. The net width of the interface in an ungrouted unit is the total thickness of the face shells of the unit and that in a grouted unit is equal to the width of the unit. The values of the modeling parameters are shown in Table 4.

Table 4 - Calibration of Interface Elements for Masonry Head Joints and Unit Interface

Wall Spec.	Joints ¹	D_{nn}, D_{tt} (MPa/mm)	s_o (MPa)	Width (mm)
1	HJ	136	0.98	51
	UI	136	1.45	68/193
3	HJ	136	0.92	51
	UI	136	1.44	68/193
5	HJ	136	1.03	51
	UI	136	1.51	68/193
7	HJ	136	0.81	51
	UI	136	1.31	68/193
9	HJ	136	0.90	51
	UI	136	1.41	68/193
11	HJ	136	0.98	51
	UI	136	1.45	68/193

¹HJ: Head Joints; UI: Unit Interface

The joints between the wall panel and the header and footer beams are assumed to have the same properties as the bed joints. The tensile strengths of the reinforcing bars are obtained from bar tests and are summarized in Table 5.

3.6. Sensitivity Analysis

Because of the large number of modeling parameters involved and the lack of experimental data to calibrate these parameters in a precise manner, a numerical parametric study

was conducted to examine the sensitivity of numerical results to these parameters. The variables studied include the tensile strength, mode-I and mode-II fracture energies, dilatancy parameter η , and shape of the yield surface (i.e., parameters μ and r) for the bed joints, the tensile strength of the head joints, and the compressive and tensile strengths of masonry. The analysis was carried out with Wall No. 1.

The results indicate that the lateral load-vs.-lateral displacement curve and failure mechanism of a partially grouted masonry shear wall are only sensitive to the shape of the yield surface, which is governed by μ and r , and not to the other parameters mentioned above. This can be attributed to the fact that the tensile strength of masonry materials is too low to have a impact on the overall load resistance of a wall. Furthermore, it has been found that while the values of fracture energies can affect the convergence of a numerical solution, they have little influence on the global response of a wall. Since the shape of the yield surface determines the Coulomb friction in a joint, the sensitivity of the numerical solutions to the yield surface indicates that the failure mechanism of the wall is very much dominated by the shearing of the bed joints.

Table 5 - Tensile Strengths of Reinforcing Bars (MPa)

Wall Spec.	No. 3	No.4	No. 5	No. 6
1	406	-	-	448
3	406	-	-	448
5	406	-	-	448
7	-	420	448	448
9	-	420	448	448
11	-	420	448	448

However, experimental data on the shear behavior of mortar joints are scarce. Mehrabi et al. [5] have tested mortar joints in $\frac{1}{2}$ -scale concrete masonry units using a direct shear machine, and have used the results to calibrate an interface model having a yield surface identical to the

one considered here. Hence, the aforementioned study provides the most relevant information for the present study, and provides guidelines for the calibration of μ and r .

4. NUMERICAL RESULTS

The lateral load-vs.-lateral deformation curves obtained for Walls No. 1, 3, 5, 7, 9, and 11 are shown in Fig. 12. It can be seen that the lower the H/L ratio of a wall is, the higher is the lateral strength. This is because the height (H) of all the walls is a constant, and, therefore, a lower H/L ratio means a longer wall. The walls with $H/L = 0.5$ demonstrate a more significant drop of post-peak resistance than the others. It can also be observed that the influence of the quantity of horizontal reinforcement in the bond beams on the load-displacement curves is almost negligible. The small influence of the horizontal steel can be explained by the failure mechanisms of the walls as described below.

Figures 13 through 18 show the deformed meshes and crack patterns for all the walls at a lateral displacement of 12.7 mm. It can be seen in Figs. 13 and 16 that the failure mechanism of the walls with $H/L = 0.5$ is dominated by the shear sliding of the bed joints adjacent to the bond beam. The crack patterns show that the behavior of such a wall is very similar to that of an infilled frame [5]. The grouted cells that contains reinforcement act like a reinforced concrete frame with two exterior columns and a horizontal beam at mid-height. The ungrouted masonry units act like infill panels which provide a diagonal strut mechanism to resist the applied lateral load. The failure of these panels is characterized by 45°-angle cracks near the compression corners and the horizontal shear sliding between the bond beam and the panels. For this reason, the Coulomb friction in the bed joints has an significant influence on the lateral resistance. Distinct vertical cracks can also be observed between the grouted and ungrouted cells near the compression corners. The frame action causes severe cracking in the two exterior columns of grouted cells. Furthermore, because of the diagonal strut action, the bond beam is subjected to a significant tension, which causes cracking in the head joints, as can be seen in the deformed mesh in Fig. 13. The cracking of the bond beam is less severe in Wall No. 7, as shown in Fig. 16, which has a higher quantity of horizontal reinforcement. In spite of this, the final failure mechanism of Wall No. 7 is still governed by the sliding shear crack and the horizontal crack at mid-height eventually propagates through one of the grouted columns.

As shown in Figs. 14 and 17, the walls with $H/L = 0.7$ essentially have the same failure mechanism as that described above. However, there is more extensive cracking in the head joints and vertical interfaces in these walls. In the walls with $H/L = 1.0$, these vertical cracks are even more wide spread, as shown in Figs. 15 and 18. In all cases, the quantity of horizontal reinforcement has little influence on the final failure mechanism, except that a higher quantity of horizontal steel reduces crack widths in the bond beam.

5. CORRELATION OF EXPERIMENTAL AND NUMERICAL RESULTS

Experimental results obtained from the wall tests have been summarized by Schultz [7]. The lateral load-vs.-lateral displacement curves obtained from the tests and analyses are compared in Figs. 19a through 24a. It can be seen that both the lateral stiffness and strength of the walls obtained in the analyses are higher than those from the tests. The peak lateral resistance of the walls is plotted against the H/L ratio in Fig. 25. The numerical results exhibit a consistent trend that the lateral strength decreases with the increase of the H/L ratio, while the experimental results are a little scattered. However, the numerical results are close to the experimental results for H/L equal to 1.0 and the best correlation is obtained for Wall No. 3. The numerical results show that the influence of the quantity of horizontal reinforcement in the bond beam on the peak resistance is small due to the failure mechanism described in the previous section. Nevertheless, the experimental results show a more distinct influence of the horizontal reinforcement than the numerical results except for the walls with the H/L of 0.7. This is because of the large resistance developed by Wall No. 3, which Schultz [7] has described as out of character for the test series. On the other hand, this wall provides that best correlation between the numerical and test results.

The aforementioned discrepancies between the test and numerical results can be attributed to several factors. First, it should be pointed out that the lateral displacements shown in Figs. 19a through 24a are based on readings obtained with the displacement transducer attached to the steel head beam. Figures 19b through 24b show the load-displacement curves based on displacements measured by the transducer attached directly to the top course of masonry right below the concrete header beam. It can be seen that the initial wall stiffness shown in these curves is a lot higher than that shown in Figs. 19a through 24a. This alludes to some possible

sliding between the steel beam and the concrete header beam or between the concrete header beam and the wall panel. Nevertheless, one should be aware of the fact that the curves shown in Figs. 19b through 24b are not reliable once the walls passed the linearly elastic stage as the masonry unit to which the transducer was attached spalled in an early stage. Furthermore, the lateral stiffness shown by the numerical results is also questionable as the shear stiffness of the mortar joints is not precisely known, and the elastic moduli of masonry are deduced from the UBC empirical formula, which provides a reasonable but not exact assessment.

The discrepancy between the lateral resistance obtained from the analyses and tests can be partly explained by the fact that the walls were subjected to cyclic loads in the tests and the analyses are carried out with monotonically increasing loads. The strength of a wall is expected to be higher under monotonically increasing loads than that under cyclic loads. Prior experimental results on fully grouted masonry walls [8] and masonry-infilled R/C frames [5] indicate that the difference in lateral resistance caused by load histories can be in the range of 10 to 20%. However, for Wall No. 1, the numerical result indicates a lateral strength that is 60% higher than the test result.

The actual failure mechanisms of Walls 1 and 3 are shown by the pictures in Fig. 26. While the failure mechanism of Wall No. 1 is representative of that of the other walls in the series, the failure mechanism of Wall No. 3 is different from the rest. Comparing the actual damage pattern of Wall No. 1 to the deformed mesh in Fig. 13a, one can see several distinctions. First, the vertical cracks between the grouted and ungrouted cells extended along the entire height of the tested wall while the deformed mesh indicates that severe vertical crack opening occurs only along one-half of the total height on each side. The anti-symmetric crack pattern shown in the numerical result is due to the fact that only a monotonically increasing load is applied in the analysis. Second, the deformed mesh shows a severe horizontal sliding right below the bond beam while no sliding is visible within the tested wall panel. These indicate the short-column effect of the exterior grouted cells in the analysis, which, therefore, results in a higher resistance. Furthermore, the wide opening of the vertical cracks in the test indicate that some sliding might occur between the concrete header beam and the wall panel. This would weaken

the resistance of the test specimen. The wide opening of the vertical cracks in the test resulted in a more severe straining of the horizontal steel in the bond beam than in the analysis.

The above explanation seems reasonable when one also compares the experimentally observed and numerically obtained damage patterns for Wall No. 3 in Figs. 14a and 26b. In this case, the vertical cracks extended only halfway along the height of the test specimen and shear sliding is evident within the panel. This experimental observation is very similar to the deformed mesh shown in Fig. 14a. Hence, it is not surprising to see that the numerical and experimental load-deformation curves are very close to each other. The “out-of-character” behavior demonstrated by Wall No. 3 could be due to an exceptionally strong bond between the panel and the concrete header beam, which could also well be the case in the finite element models.

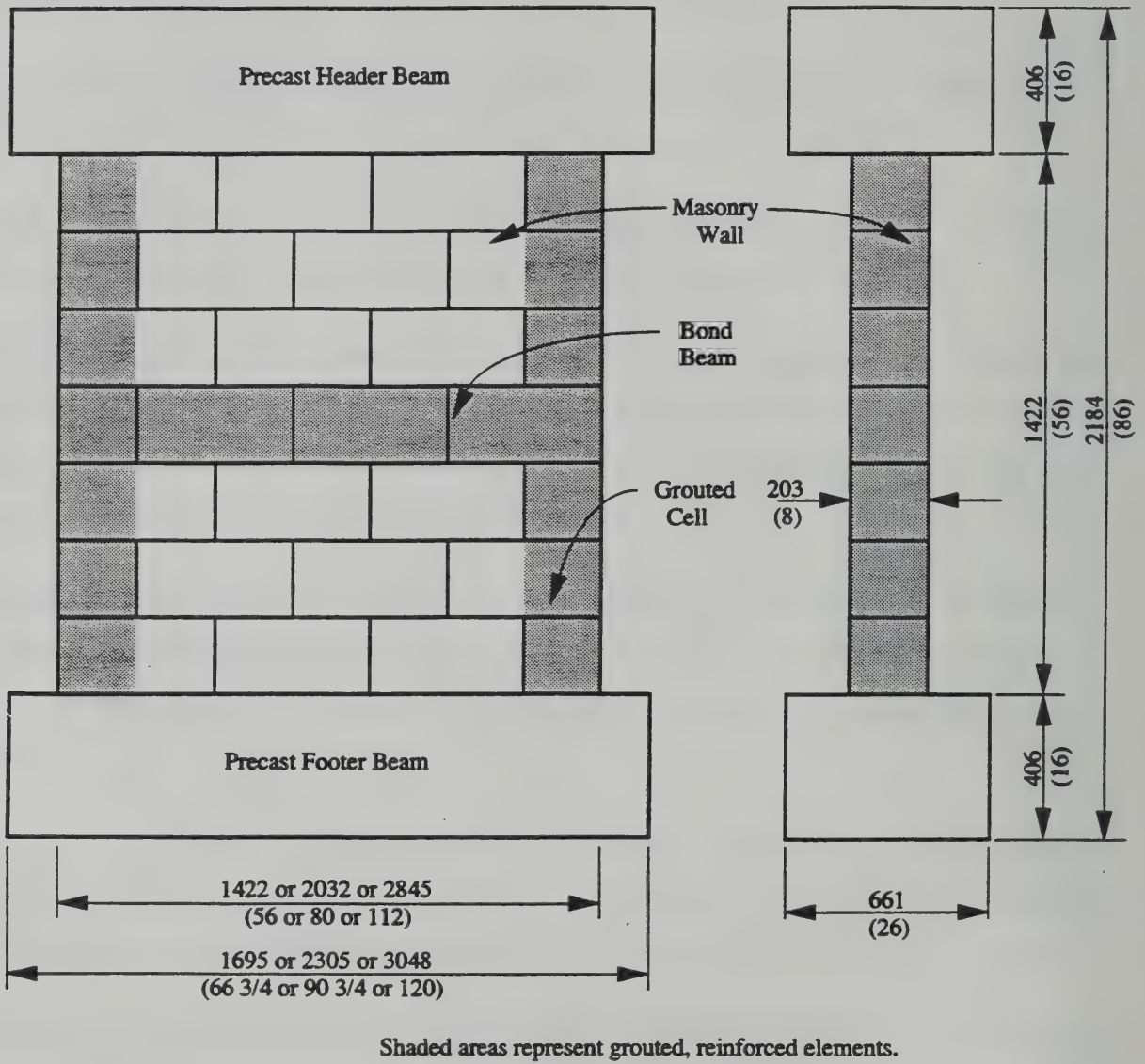
6. CONCLUSIONS

This study shows that the behavior of a partially grouted reinforced masonry wall is very similar to that of a reinforced concrete infilled frame. The grouted masonry provides the frame action while the ungrouted masonry acts like infill panels. Because of the diagonal strut action of the ungrouted masonry panels, the bond beam can be subjected to severe tension, which can lead to the fracture of the interfaces between the bond beam and the exterior columns of grouted cells. However, as long as the horizontal steel is of sufficient quantity to prevent the tension failure of the bond beam, the variation of its quantity seems to have a small influence on the behavior of the wall panels. The walls with a low aspect ratio tend to exhibit a distinct sliding shear failure through the bed joints at mid-height, while those with a higher aspect ratio have more severe cracking in the vertical joints within the panels. The vertical cracks between the grouted and ungrouted cells are reasonably well captured in the analyses. Except for one wall specimen, the lateral strengths obtained in the analyses are higher than those shown by the tests. The discrepancies in the numerical and experimental load-displacement curves can be partly caused by the different load histories (namely, monotonically increasing and cyclic) and partly by the discrepancy in the bond strength between the wall panels and the concrete head beams.

7. REFERENCES

1. Ewing, R.D., El-Mustapha, A.M., and Kariotis, J.C., "A Finite Element Computer Program for the Nonlinear Static Analysis of Reinforced Masonry Walls," *Proceedings, Eight International Brick/Block Masonry Conference*, Dublin, Ireland, 1988.
2. Lotfi, H.R. and Shing, P.B., "An Appraisal of Smeared Crack Models for Masonry Shear Wall Analysis," *Computers & Structures*, Vol. 41, No. 3, pp. 413-425, 1991.
3. Lotfi, H.R. and Shing, P.B., "Interface Model Applied to Fracture of Masonry Structures," *Journal of Structural Engineering*, ASCE, Vol. 120, No. 1, pp. 63-80, 1994.
4. Manzouri, T., Shing, P.B., Amadei, B., Schuller, M.P., and Atkinson, R.H., "Repair and Retrofit of Unreinforced Masonry Walls: Experimental Evaluation and Finite Element Analysis," *Report No. CU/SR-95/2*, Department of Civil, Environmental, and Architectural Engineering, University of Colorado, Boulder, CO, 1995.
5. Mehrabi, A.B., Shing, P.B., Schuller, M.P., and Noland, J.L., "Performance of Masonry-Infilled R/C Frames under In-Plane Lateral Loads," *Report No. CU/SR-94/6*, Department of Civil, Environmental, and Architectural Engineering, University of Colorado, Boulder, CO, 1994.
6. Schultz, A.E., "NIST Research Program on the Seismic Resistance of Partially-Grouted Masonry Shear Walls," *Report No. NISTIR 5481*, Building and Fire Research Laboratory, National Institute of Standards and Technology, Gaithersburg, MD, 1994.
7. Schultz, A.E., "Seismic Resistance of Partially-Grouted Masonry Shear Walls," in *Worldwide Advances in Structural Concrete and Masonry*, AE. Schultz and S.L. McCabe (Ed.), Proceedings of CCMS Symposium (ASCE Structures Congress XIV), Chicago, IL, 1996, pp. 211-222.
8. Shing, P.B., Noland, J.L., Spaeh, H.P., Klammerus, E.W., and Schuller, M.P., "Response of Single-Story Reinforced Masonry Shear Walls to In-Plane Lateral Loads," *Report No. 3.1(a)-*

- 2, U.S.-Japan Coordinated Program for Masonry Building Research, Department of Civil, Environmental, and Architectural Engineering, University of Colorado, Boulder, CO, 1991.
9. *Uniform Building Code*, International Conference of Building Officials, Whittier, CA, 1991.

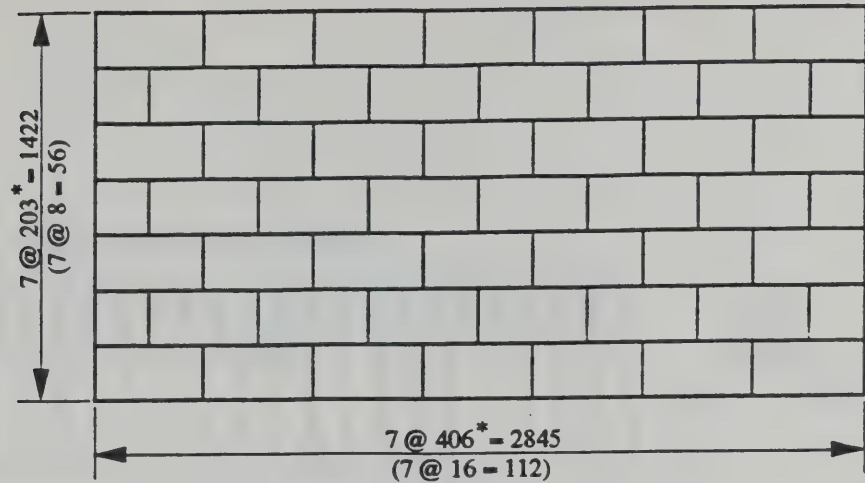


a) Elevation

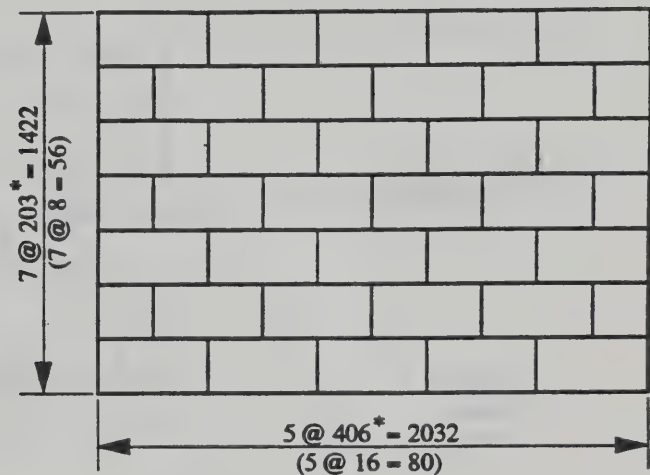
b) Side View

Fig. 1 - Partially Grouted Reinforced Masonry Wall Specimen [Ref. 6]

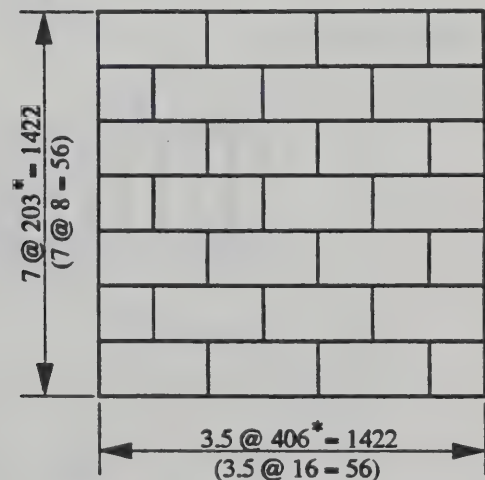
a) $r = 0.5$



b) $r = 0.7$



c) $r = 1.0$



*Masonry unit plus one bed joint and one head joint is 203 mm (8 in.) tall and 406 mm (16 in.) long.

Fig. 2 - Dimensions of Masonry Wall Specimens [Ref. 6]

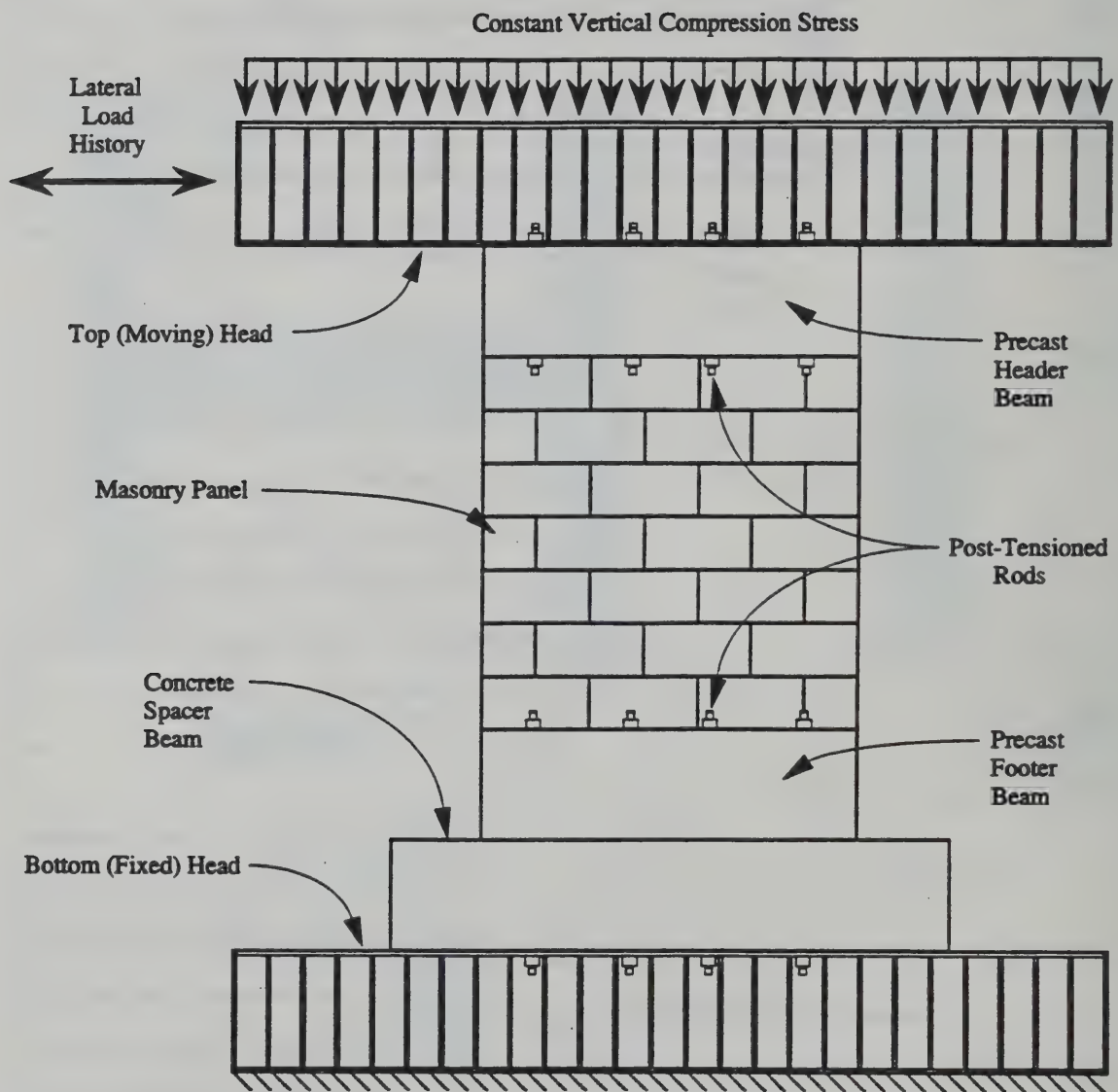


Fig. 3 - Test Setup [Ref. 6]

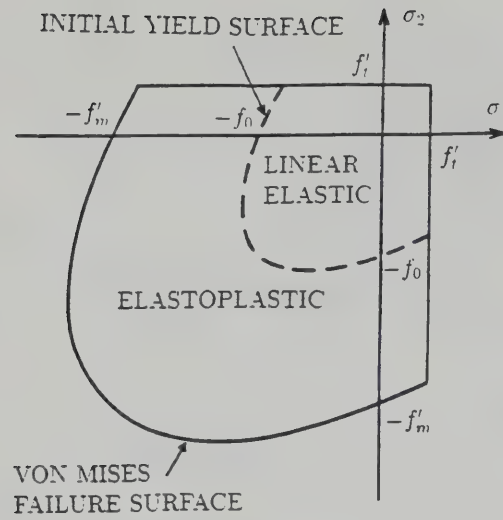


Fig. 4 - Yield and Failure Surfaces for Smeared Crack Model

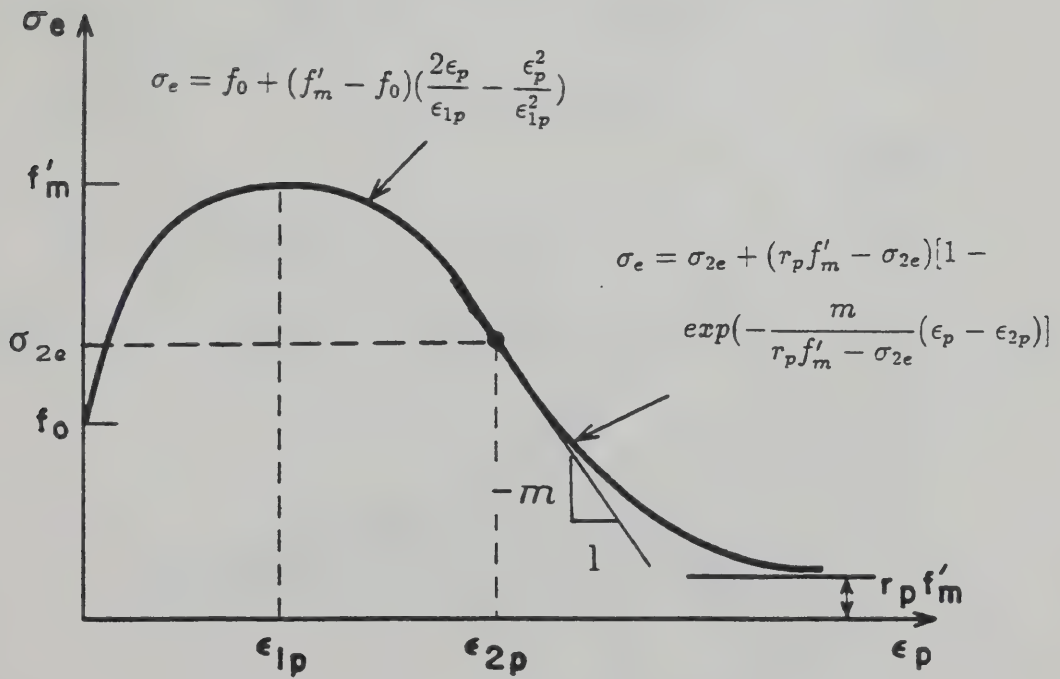


Fig. 5 - Effective Stress-Effective Plastic Strain Relation

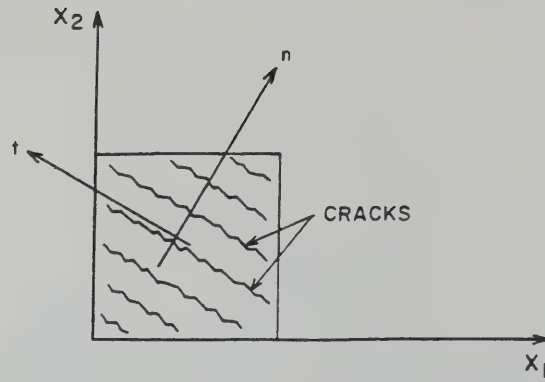
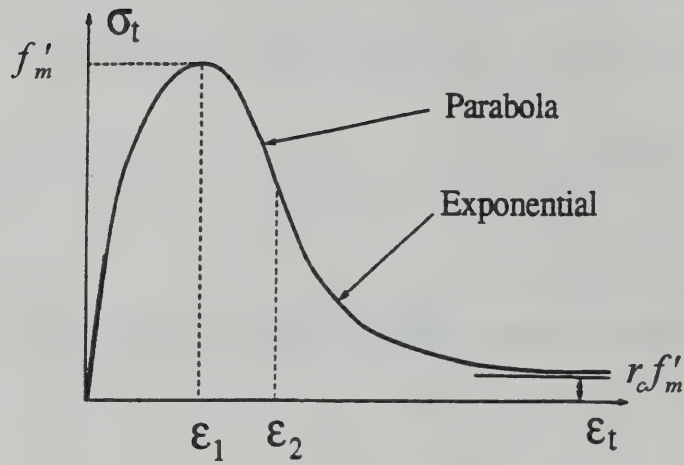
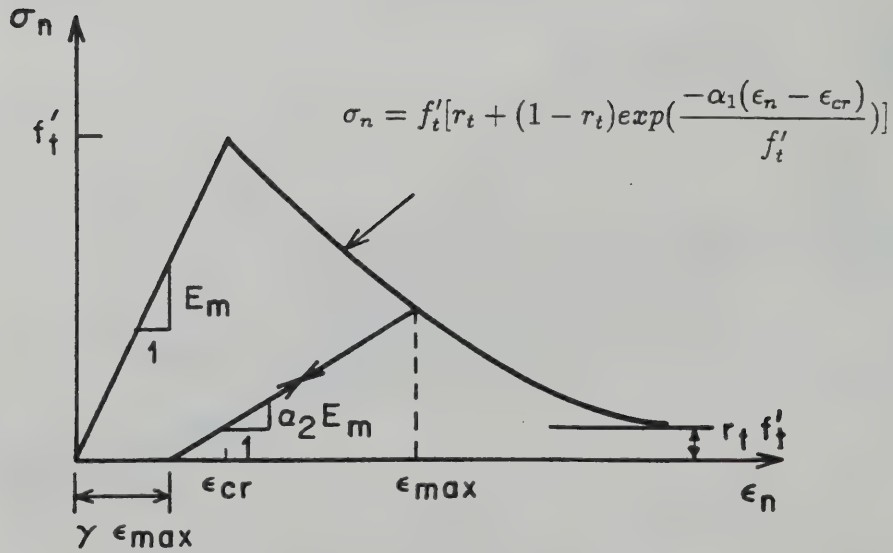


Fig. 6 - Smeared Cracks



(a) Compressive Behavior



(b) Tensile Behavior

Fig. 7 - Orthotropic Material Model

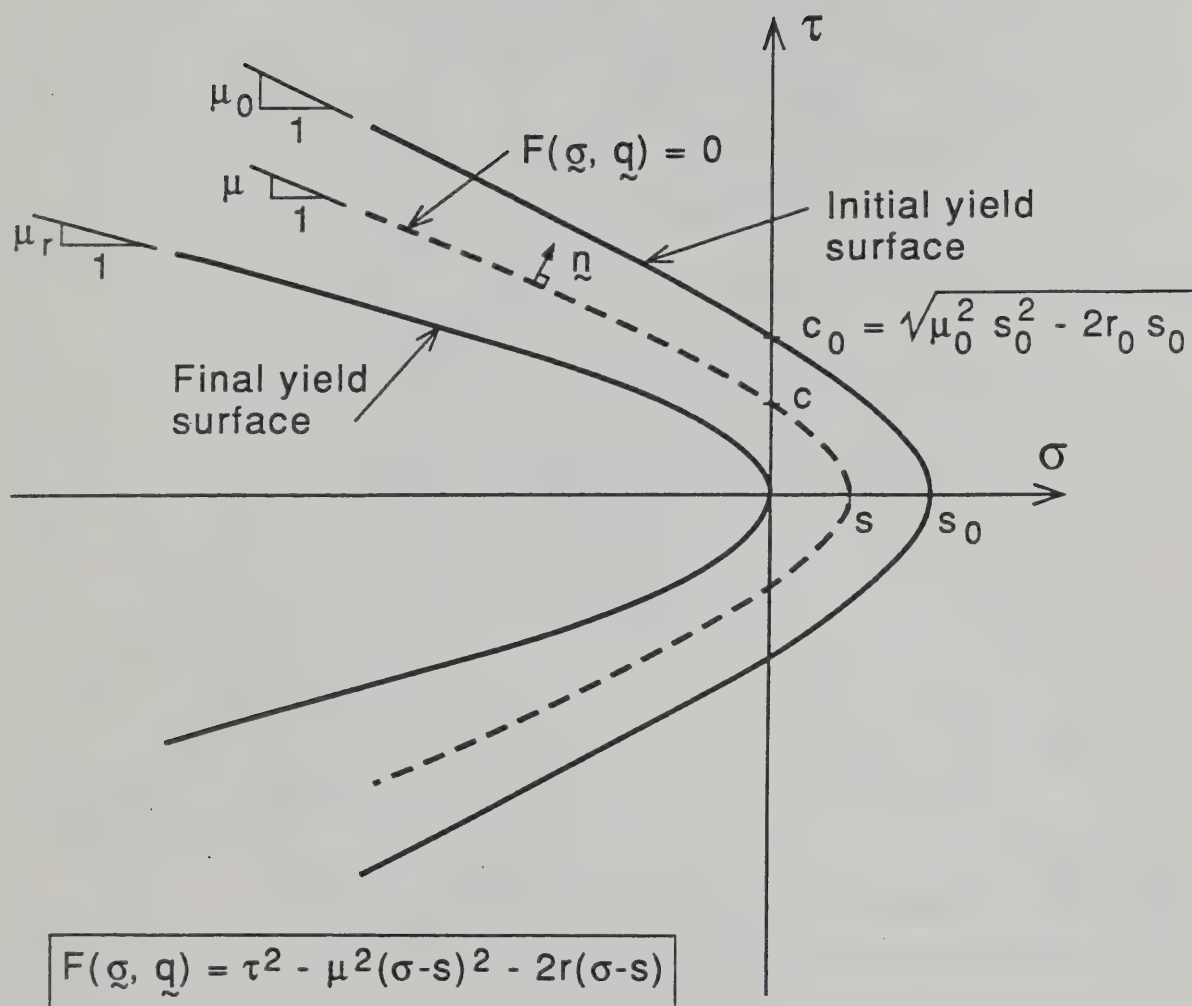


Fig. 8 - Yield Surface of Interface Model

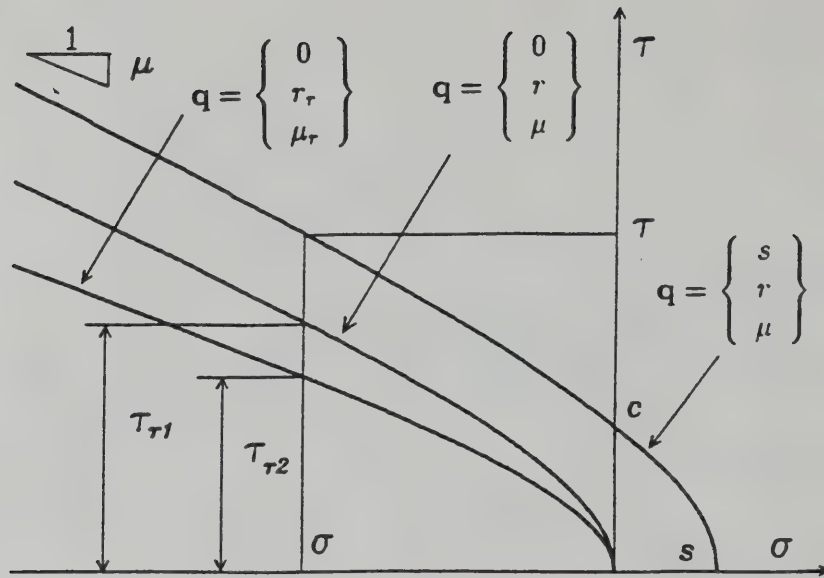


Fig. 9 - Residual Shear Strength of Interface

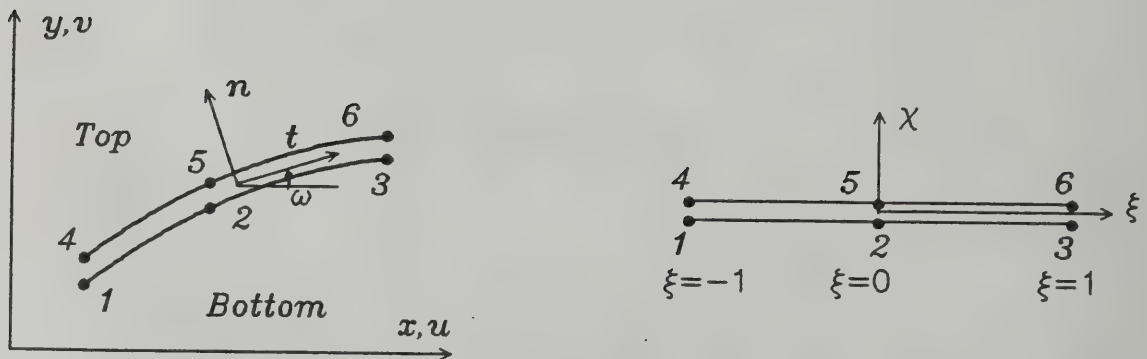
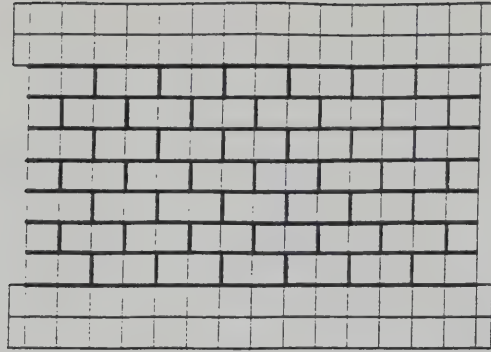
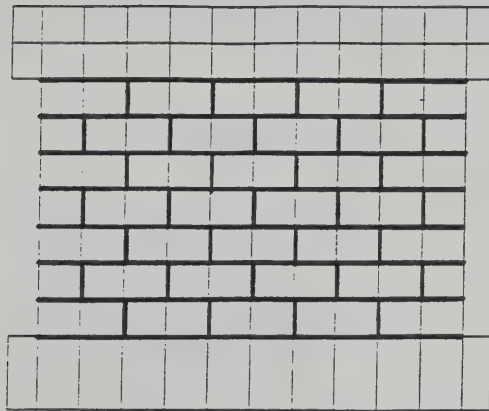


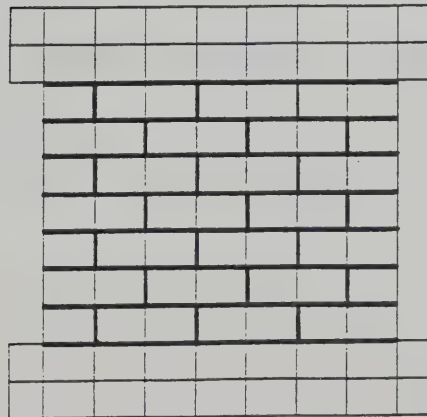
Fig. 10 - Interface Element



(a) Walls No. 1 and 7



(b) Walls No. 3 and 9



(c) Walls No. 5 and 11

Fig. 11 - Finite Element Meshes for Wall Specimens

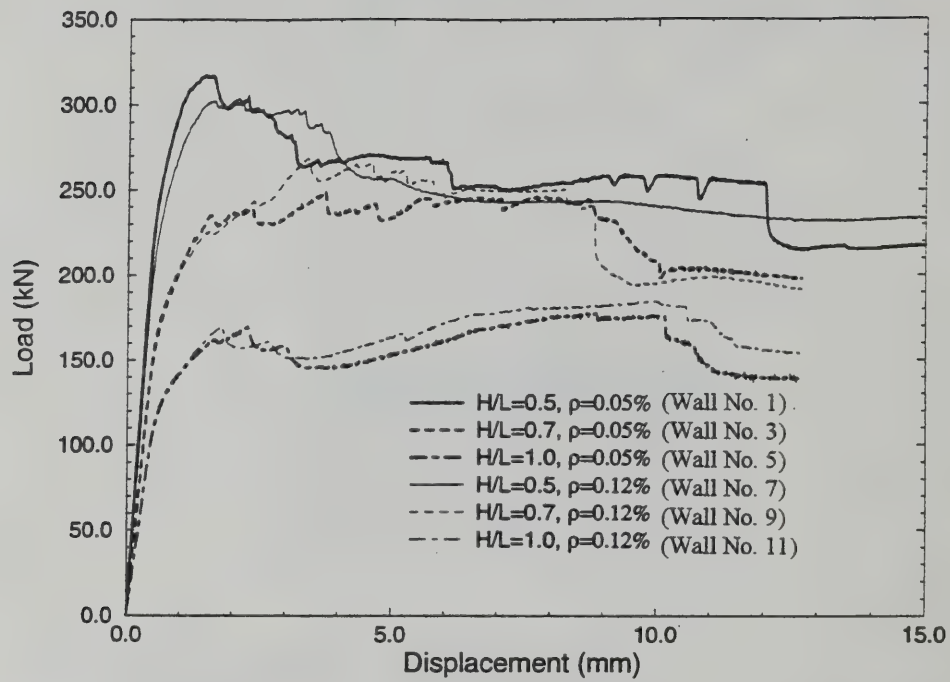
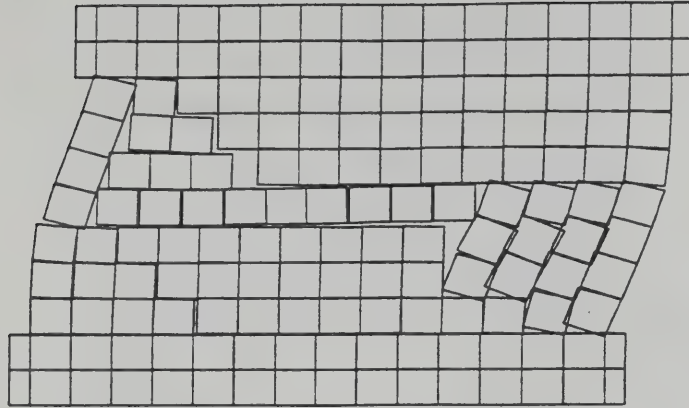
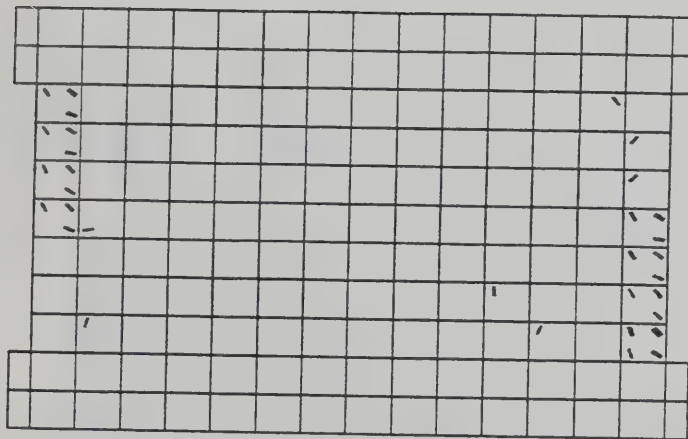


Fig. 12 - Lateral Load-vs.-Lateral Displacement Curves

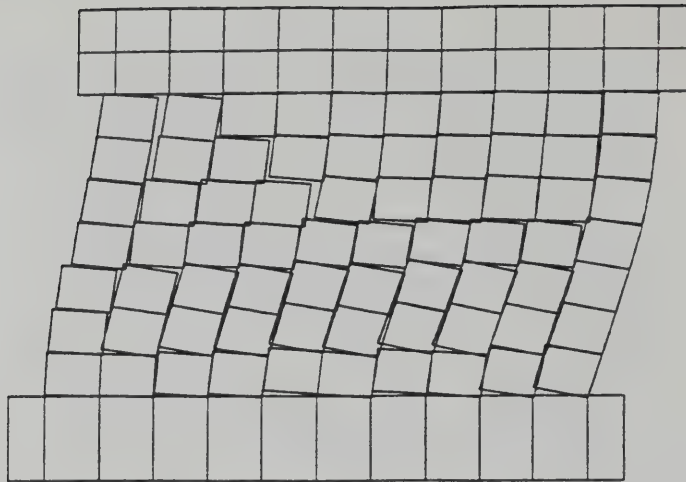


(a) Deformed Mesh

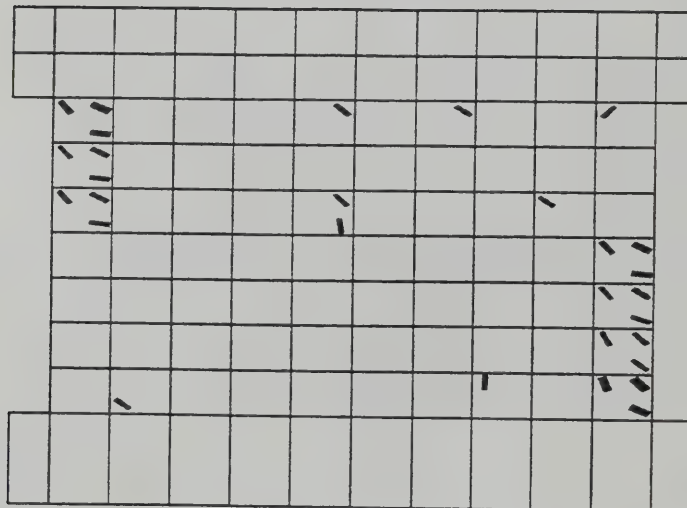


(b) Crack Pattern

Fig. 13 - Deformed Mesh and Crack Pattern for Wall No. 1 at Displacement = 12.7 mm

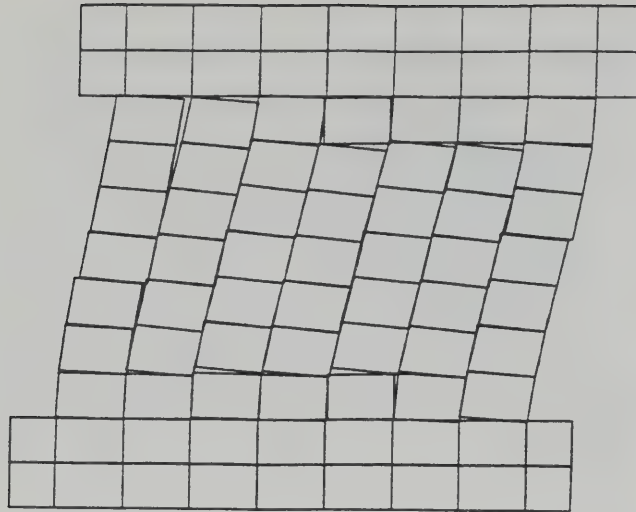


(a) Deformed Mesh

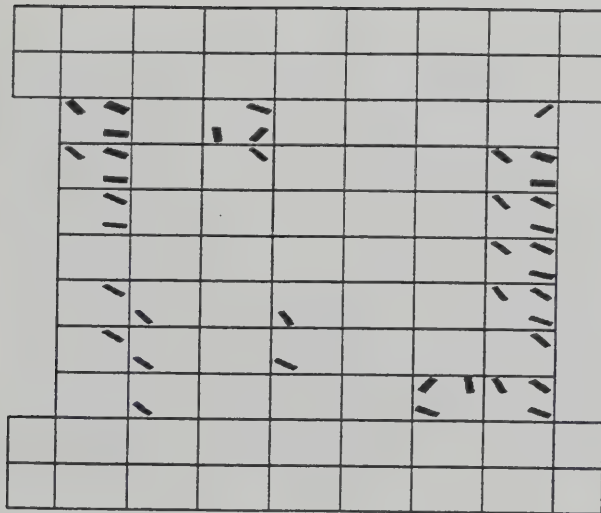


(b) Crack Pattern

Fig. 14 - Deformed Mesh and Crack Pattern for Wall No. 3 at Displacement = 12.7 mm

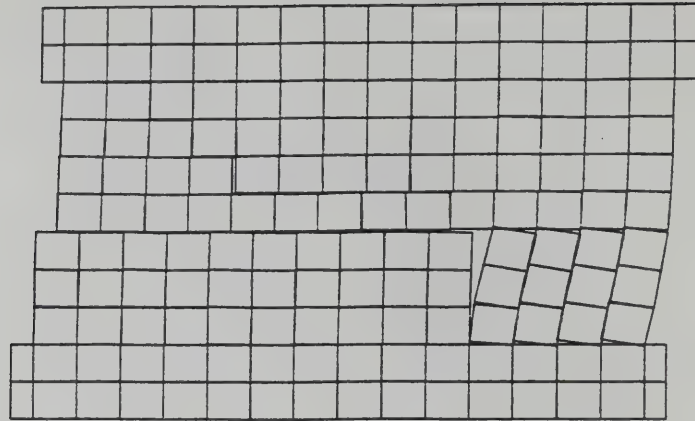


(a) Deformed Mesh

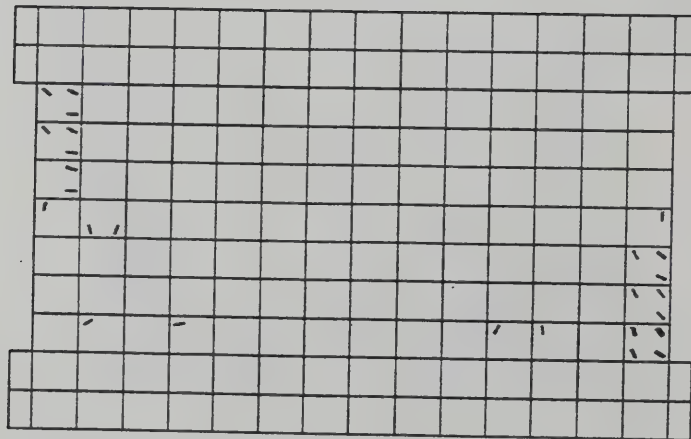


(b) Crack Pattern

Fig. 15 - Deformed Mesh and Crack Pattern for Wall No. 5 at Displacement = 12.7 mm

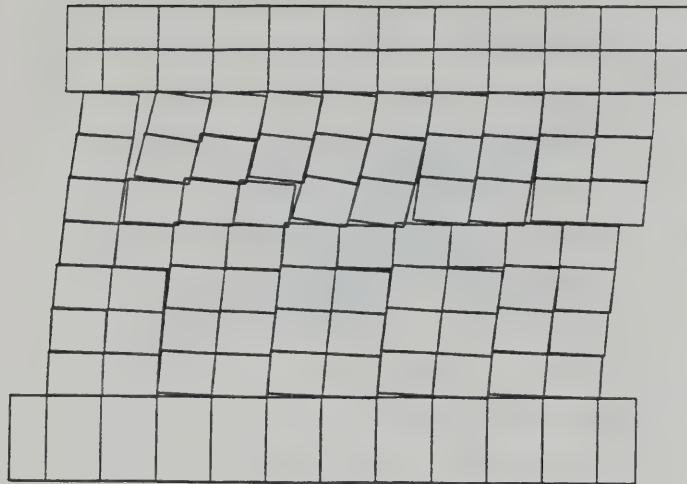


(a) Deformed Mesh

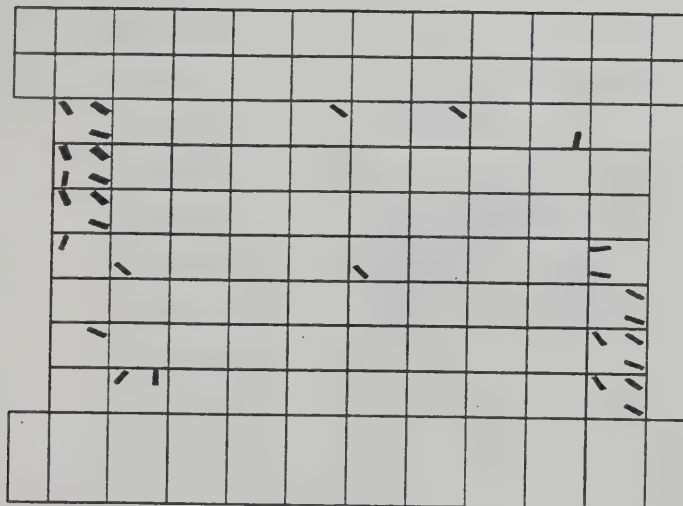


(b) Crack Pattern

Fig. 16 - Deformed Mesh and Crack Pattern for Wall No. 7 at Displacement = 12.7 mm

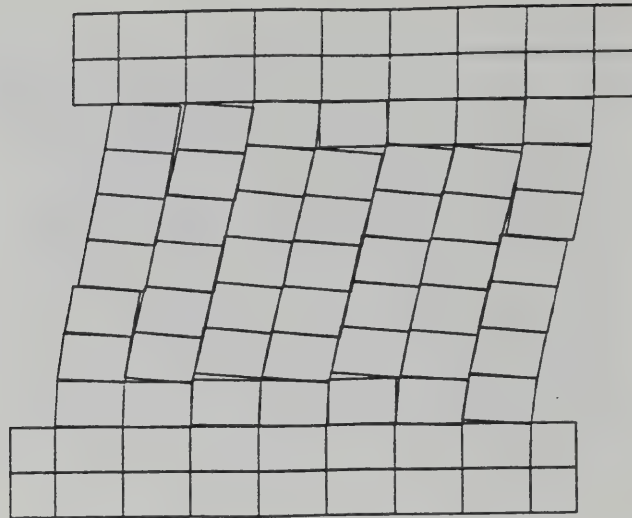


(a) Deformed Mesh

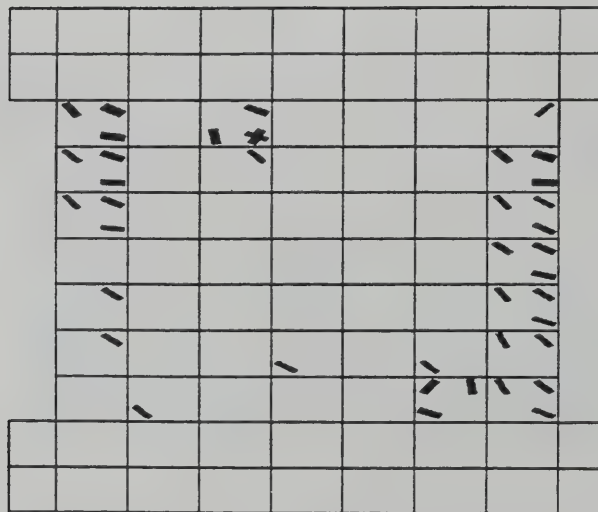


(b) Crack Pattern

Fig. 17 - Deformed Mesh and Crack Pattern for Wall No. 9 at Displacement = 12.7 mm

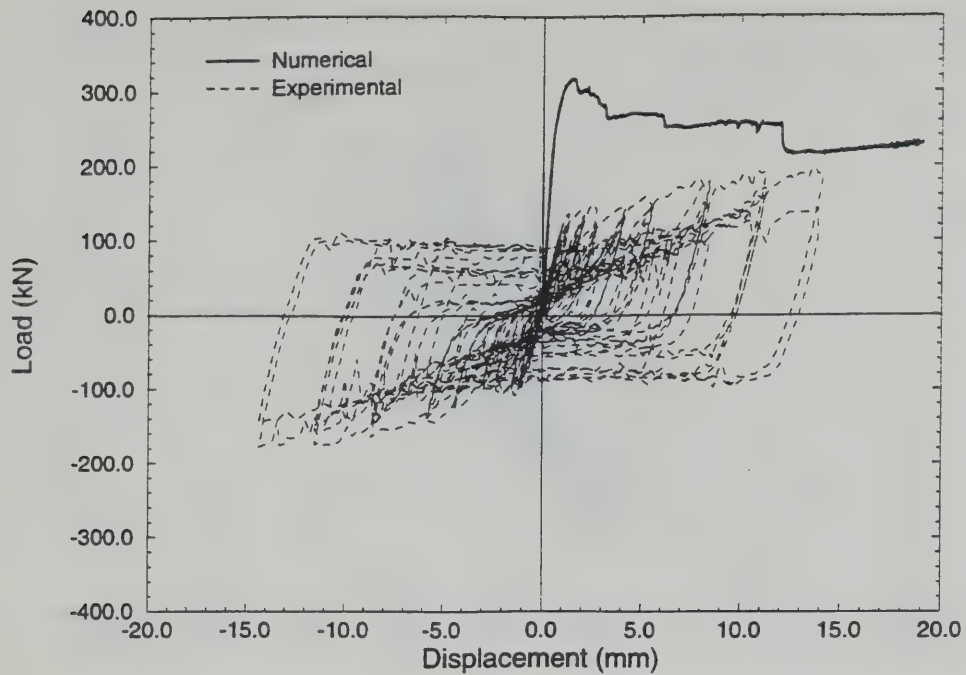


(a) Deformed Mesh

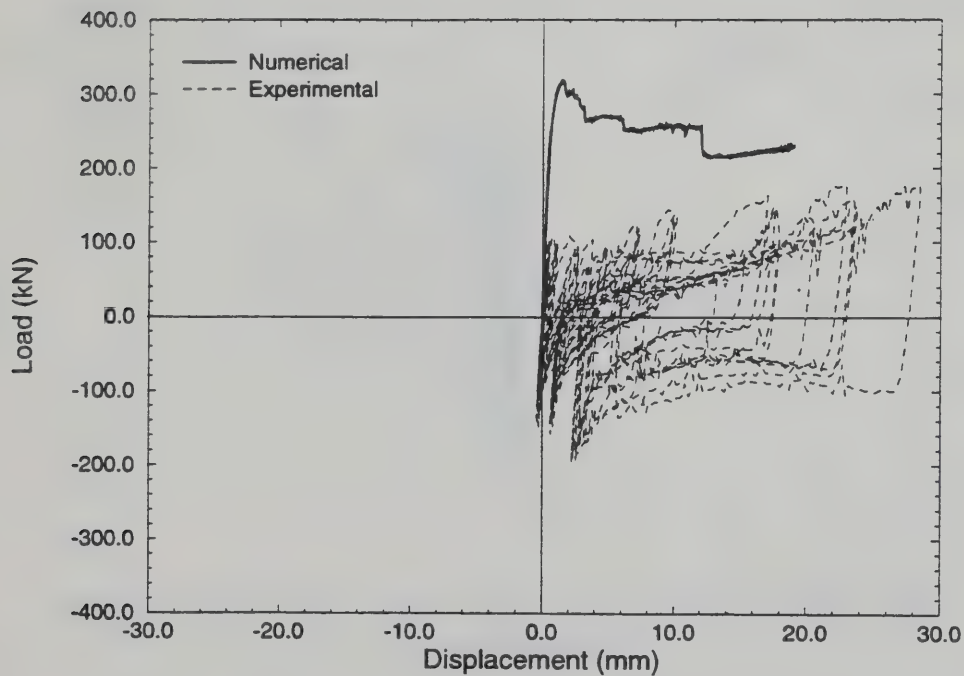


(b) Crack Pattern

Fig. 18- Deformed Mesh and Crack Pattern for Wall No. 11 at Displacement = 12.7 mm

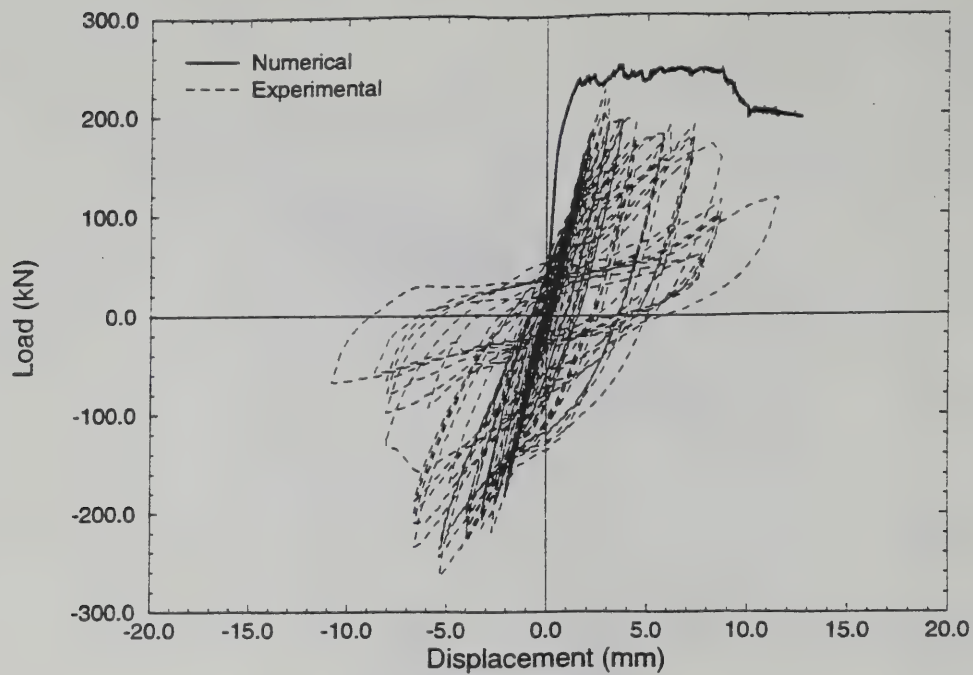


(a) Displacement Measured at Steel Top Head Beam

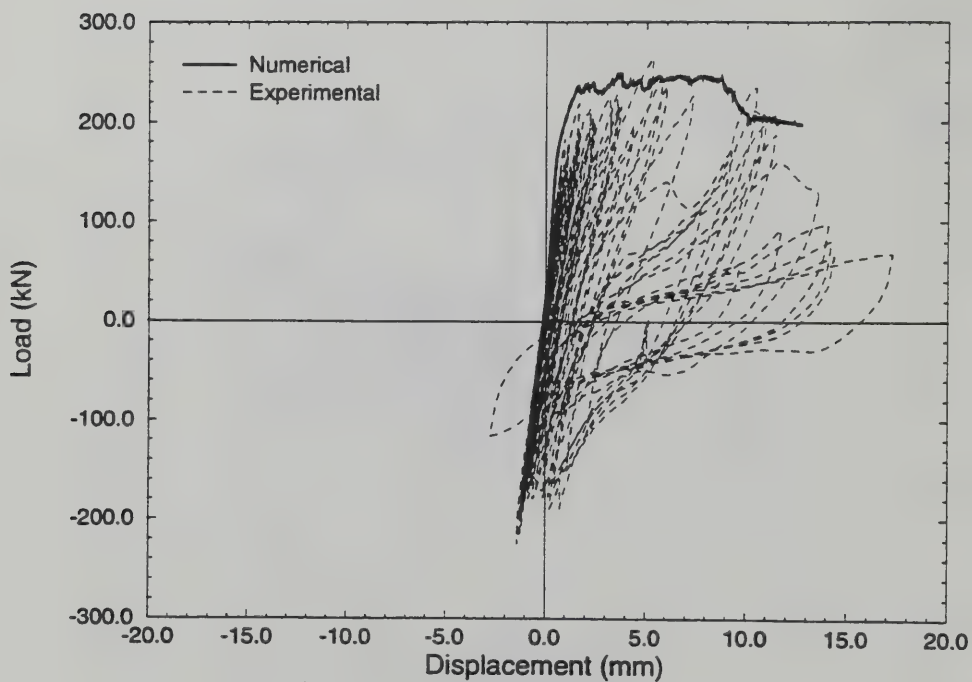


(b) Displacement Measured at Top Masonry Course

Fig. 19 - Comparison of Experimental and Numerical Results for Wall No. 1

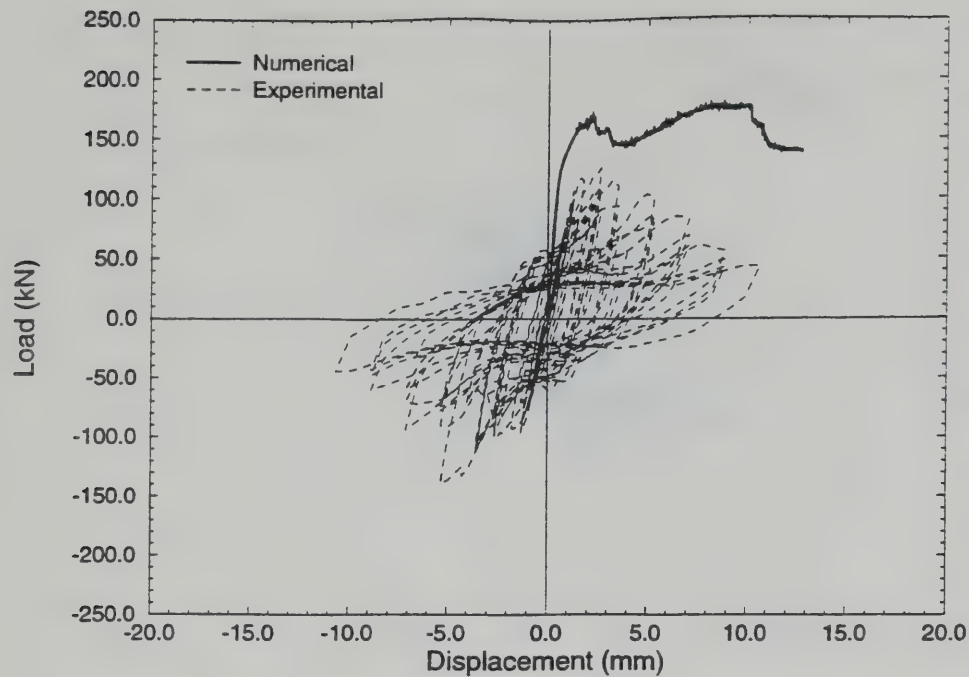


(a) Displacement Measured at Steel Top Head Beam

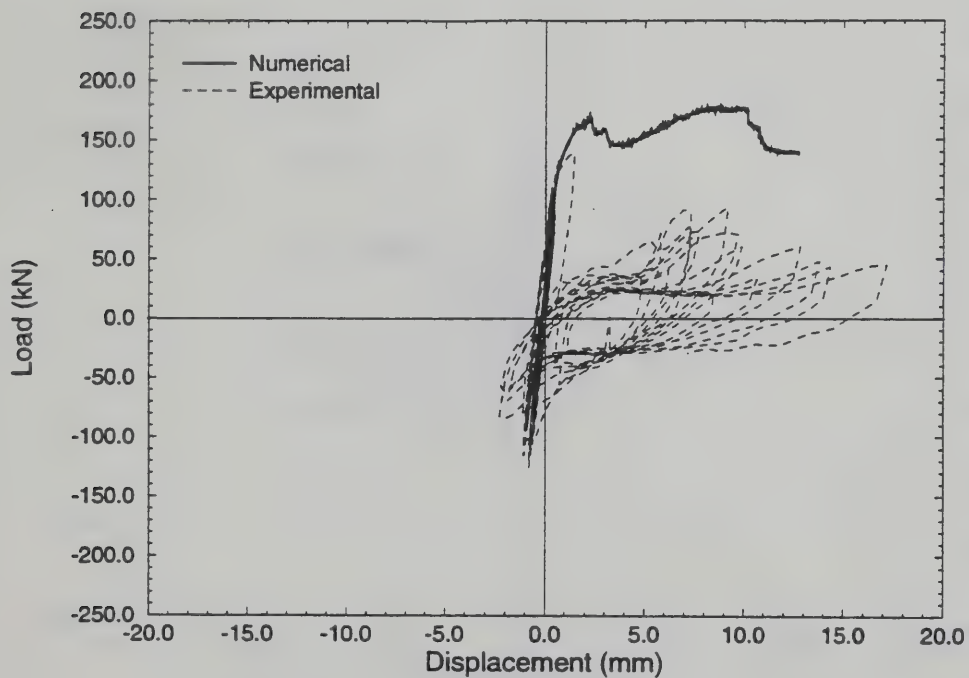


(b) Displacement Measured at Top Masonry Course

Fig. 20 - Comparison of Experimental and Numerical Results for Wall No. 3

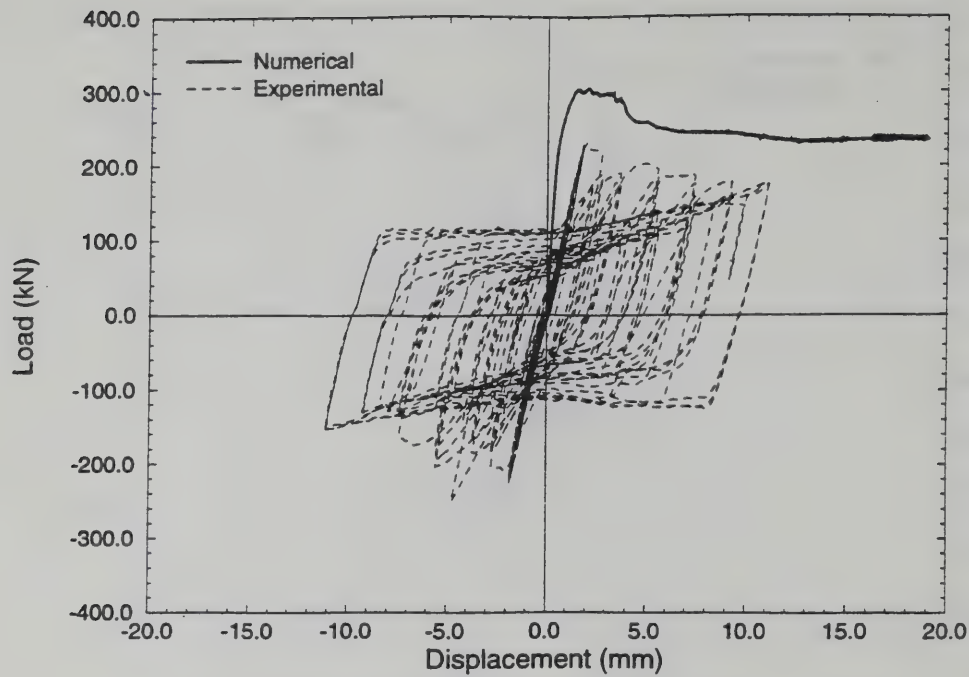


(a) Displacement Measured at Steel Top Head Beam

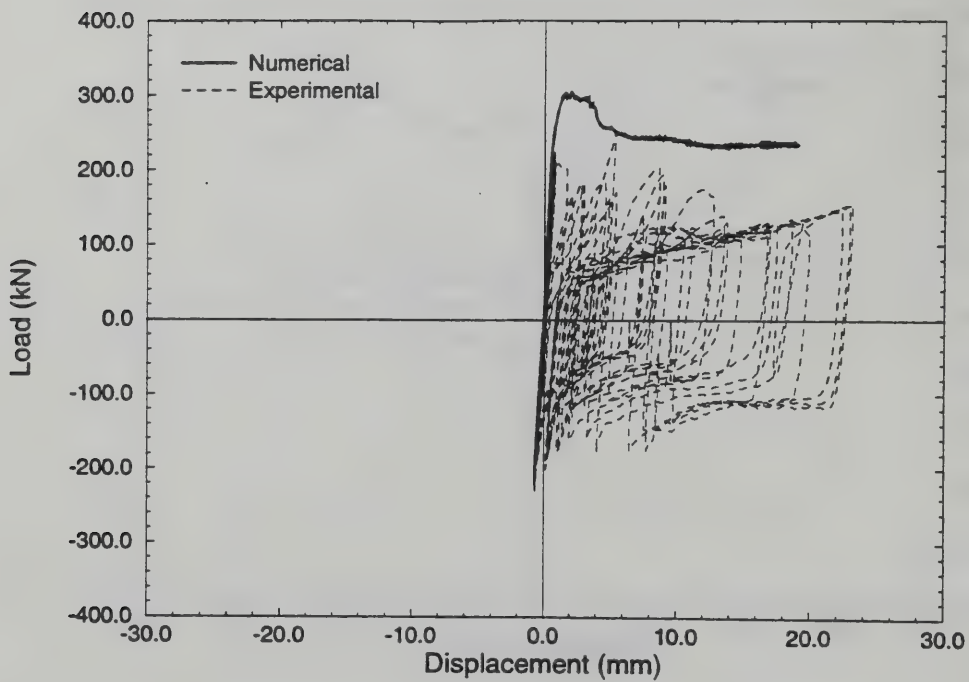


(b) Displacement Measured at Top Masonry Course

Fig. 21 - Comparison of Experimental and Numerical Results for Wall No. 5

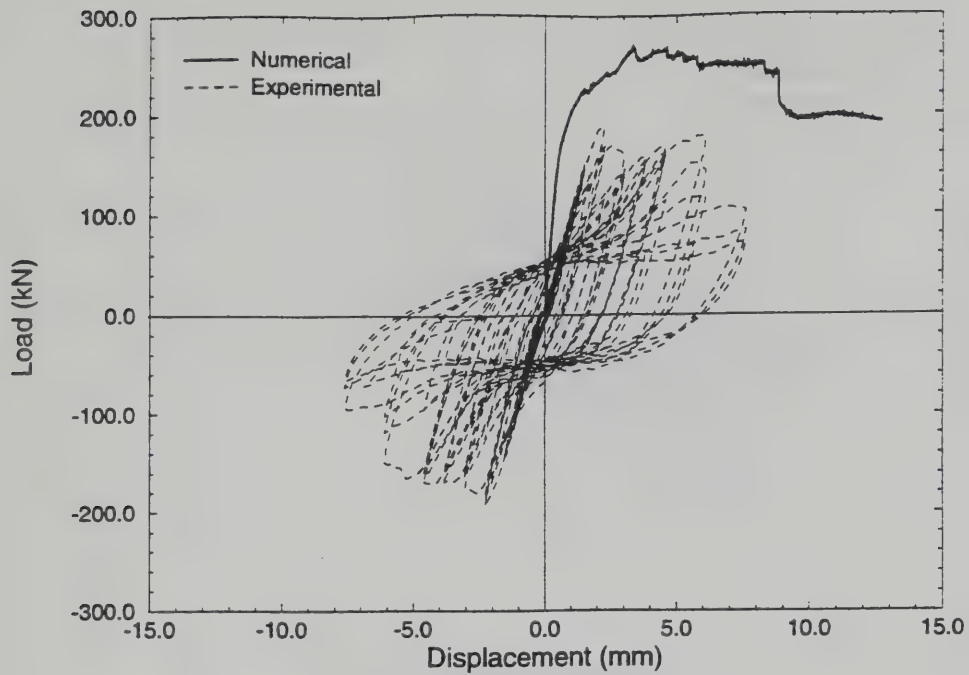


(a) Displacement Measured at Steel Top Head Beam

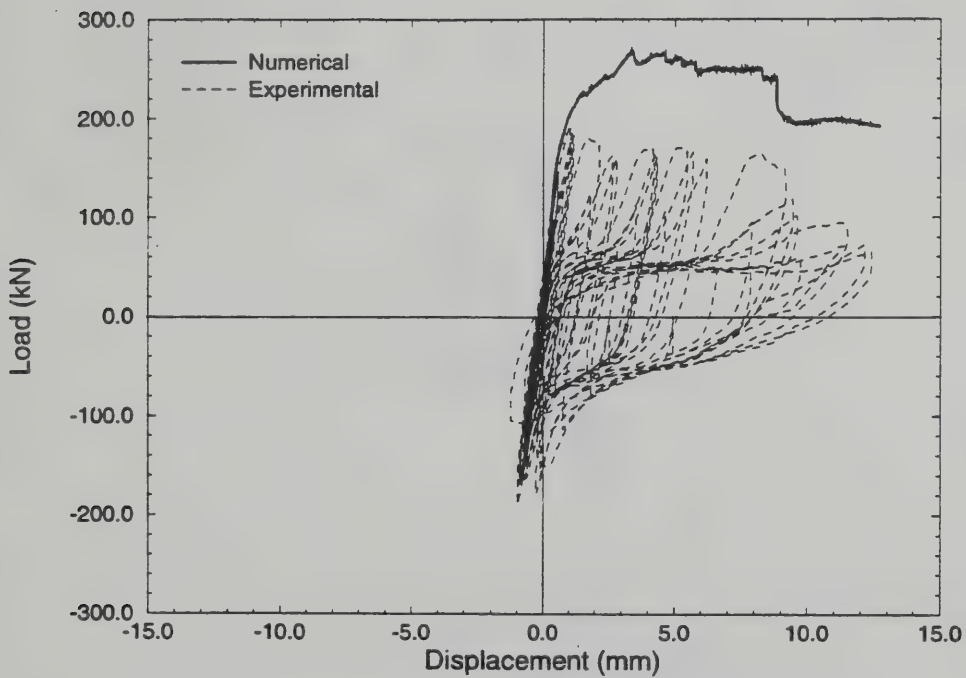


(b) Displacement Measured at Top Masonry Course

Fig. 22 - Comparison of Experimental and Numerical Results for Wall No. 7

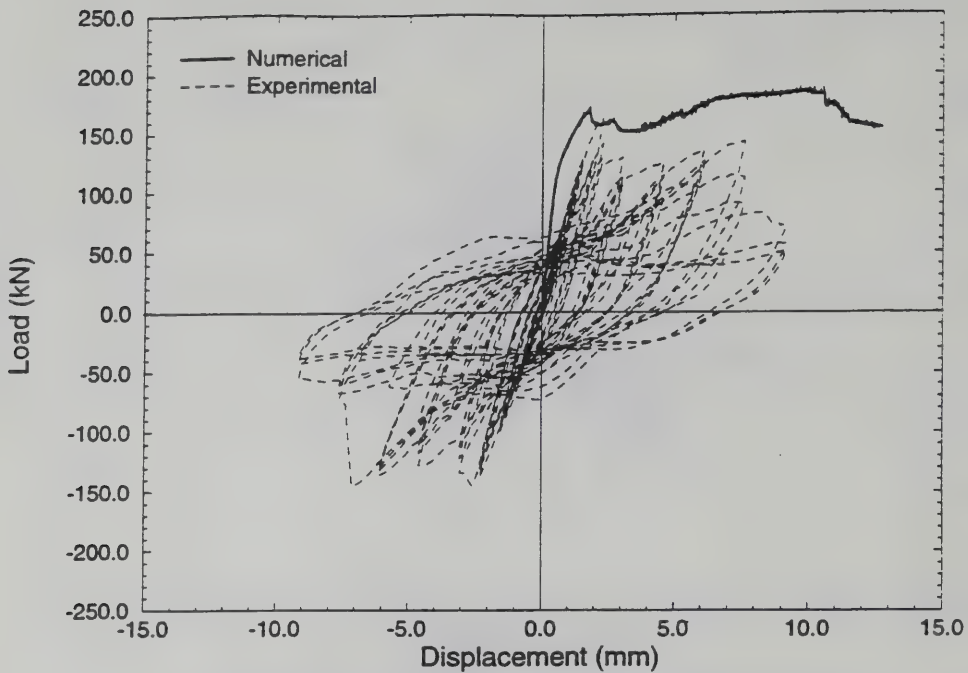


(a) Displacement Measured at Steel Top Head Beam

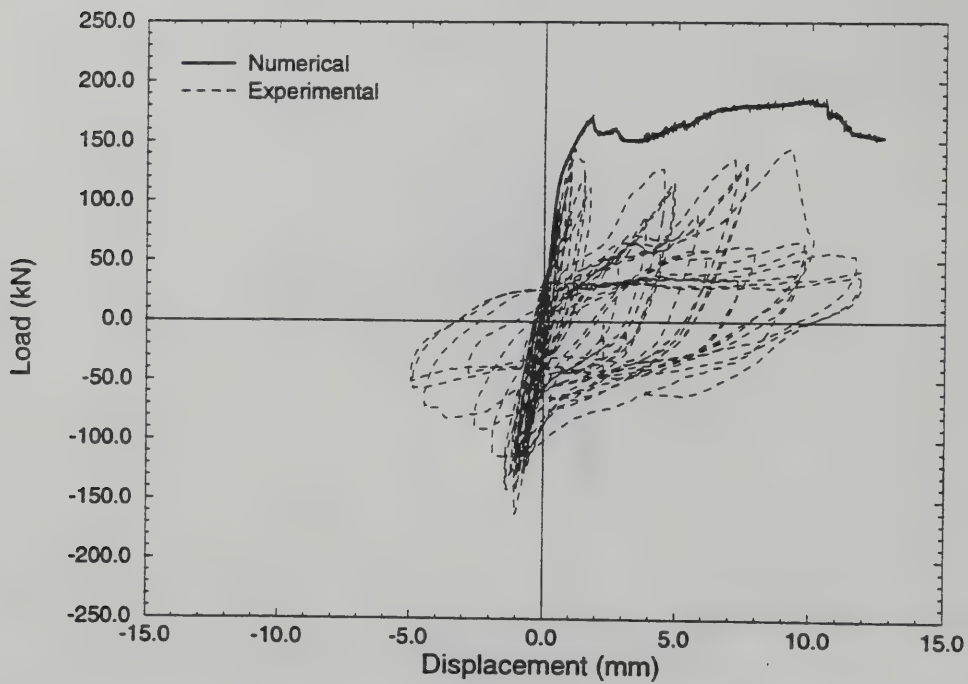


(b) Displacement Measured at Top Masonry Course

Fig. 23 - Comparison of Experimental and Numerical Results for Wall No. 9



(a) Displacement Measured at Steel Top Head Beam



(b) Displacement Measured at Top Masonry Course

Fig. 24 - Comparison of Experimental and Numerical Results for Wall No. 11

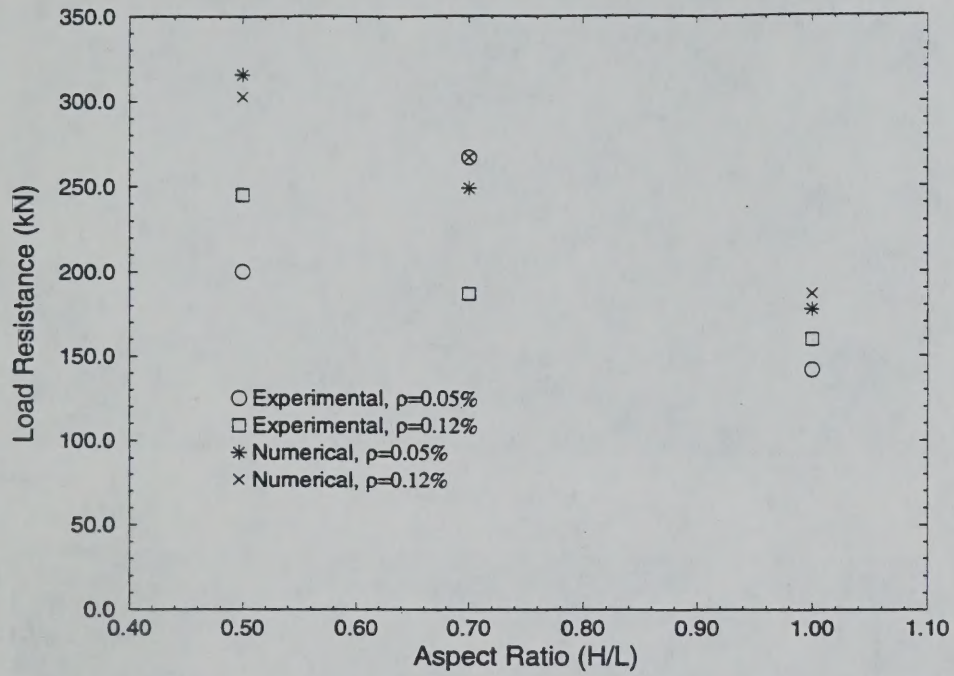
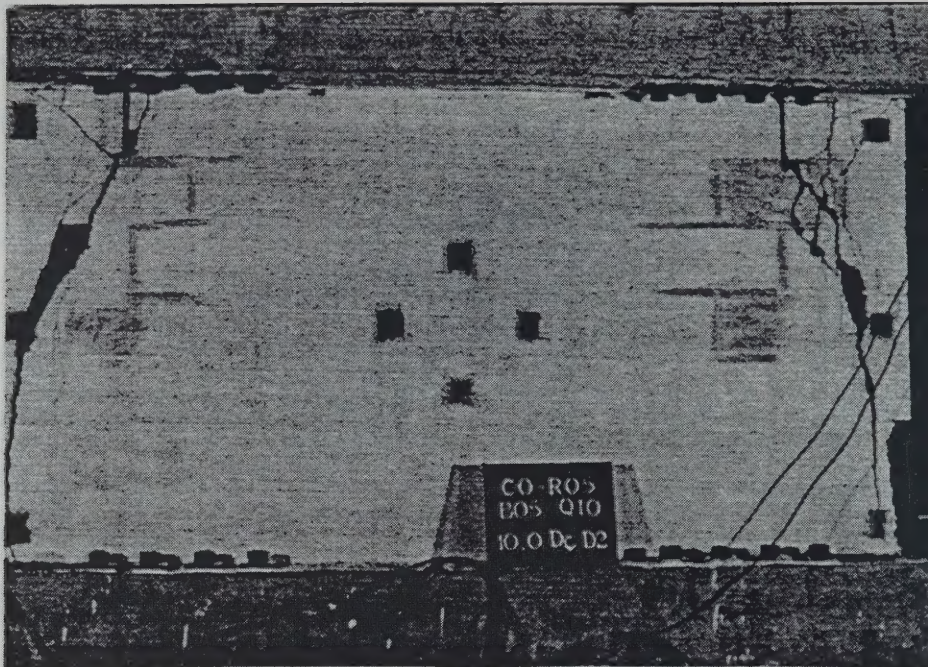
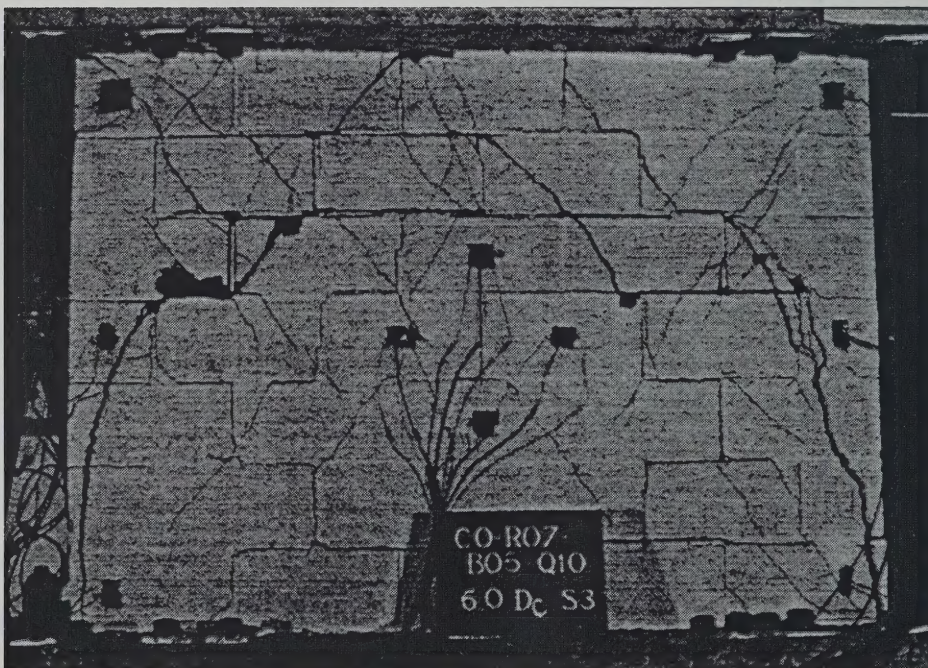


Fig. 25 - Influence of Aspect Ratio and Horizontal Reinforcement on Lateral Resistance



(a) Wall No. 1



(b) Wall No. 3

Fig. 26 - Damage Patterns from Experiments

